RESEARCH ARTICLE

Adaptive Parameter Selection Variational Mode Decomposition Based on Bayesian Optimization and Its Application to the Detection of ITSC in PMSM

YAN-KUN XIA[iD], WAN-TING WANG, AND XIN-YANG LI[iD]

School of Electrical and Electronic Information Engineering, Xihua University, Chengdu 610039, China

Corresponding author: Yan-Kun Xia (yankunjtdx@126.com)

ABSTRACT Permanent magnet synchronous motor (PMSM) is a vital component of modern industry which is widely used in transport, aerospace and intelligent machinery. In the light of its relatively high frequency of inter-turn short circuit (ITSC) fault, it is valuable to detect the fault accurately and efficiently. Due to the convenience of motor vibration signal measurement, more attention has been paid to fault detection methods based on vibration signal. As a nonstationary, nonlinear signal, vibration signal is highly susceptible to external noise interference. Variational mode decomposition (VMD) has a wide range of applications in the field of nonlinear signal analysis, but the processing ability to the signal is affected by the parameter setting. Hence, a Bayesian optimized adaptive parameter selection variational mode decomposition (BOAPS-VMD) signal processing method is proposed and applied to detect the ITSC in PMSM. Firstly, the motor vibration signal is decomposed through BOAPS-VMD, and the intrinsic mode functions (IMFs) are obtained. Secondly, the cumulative variance contribution rate (C-VCR) is applied to identify the IMFs that contain fault signature information. Finally, using Hilbert transform (HT) to further analyze the IMFs that are identified. The results are output in 3D time-frequency diagrams to enhance the representation of fault signatures. The effectiveness and accuracy of the BOAPS-VMD were validated through the finite element simulation and experiment. The study shows that the BOAPS-VMD effectively improves the modal mixing phenomenon, has better noise robustness, improves the accuracy of fault detection, and has better engineering applicability.

INDEX TERMS Permanent magnet synchronous motor (PMSM), fault detection, variational mode decomposition (VMD), Bayesian optimization, Hilbert transform (HT).

I. INTRODUCTION

Permanent magnet synchronous motors (PMSMs) are typically used in a variety of industrial applications where the operating environment is relatively severe. The severe operating conditions could shorten their service life or lead to premature damage. Statistics show that short circuit faults are more likely to occur among the motor faults [1], [2], [3], [4], [5]. PMSMs usually operate with high loads for long periods, and the body temperature is usually high, which tend

to reduce the insulation in the stator winding coils. After that, the inter-turn short circuit (ITSC) occurs. It is worth noting that this fault could further lead to the ground short circuit in the PMSM, causing the motor temperature to rise continuously. In the end, the motor is burnt out, causing serious financial losses. Therefore, to ensure reliable system operation, the study of corresponding short circuit fault detection techniques is of irreplaceable value.

The comprehensive reviews of motor fault detection techniques are given in [6], [7], [8], [9], and [10]. In recent years, fault detection techniques based on signal processing have been increasingly used, such as frequency domain analysis,

The associate editor coordinating the review of this manuscript and approving it for publication was Mehrdad Saif[iD].

time domain analysis, and frequency-time analysis [11], [12], [13], [14], [15]. Reference [16] detected the motor fault using wavelet packet transform (WPT) and modified Hilbert transform (HT). However, it did not discuss the accuracy of fault detection under complex operating conditions. Reference [17] obtained the motor phase voltage spectrums using the fast Fourier transform (FFT). Finally, the fault was identified by linear discriminant analysis. All of the above fault detection techniques have some engineering reference value.

A PMSM with an ITSC will show a significant change in its vibration intensity. Therefore, by analyzing the signatures of the vibration signal, it is possible to detect the motor fault. The vibration signal of the PMSM has non-stationary, nonlinear characteristics [18]. In recent years, signal processing methods based on nonlinear dynamics have been widely used in rotating machinery fault detection. Reference [19] introduced the sea-horse optimizer into the threshold adjustment of slope entropy and further proposed an optimized multivariate multiscale slope entropy. Reference [20] proposed a refined composite variable-step multiscale multimapping dispersion entropy, which exhibits better information extraction ability for time series. Reference [21] proposed a variable-step multiscale single threshold slope entropy and introduced the snake optimizer into the threshold adjustment of the slope entropy.

In the field of fault detection, the accuracy of fault feature extraction is of great importance. HT transforms a signal from the time domain to the frequency domain. It provides a detailed analysis of how the signal changes in time and frequency. In addition, HT has the advantages of multi-scale, high resolution, and high sensitivity. It is now used in a large number of applications for fault detection [22], [23], [24]. Therefore, HT can be used to analyze the motor vibration signal and detect the ITSC in PMSM. However, HT is sensitive to noise and also has disadvantages such as endpoint effects. As a result, the fault signatures obtained from direct analysis of the vibration signal using HT are often less accurate. To achieve a better analysis of the signal, researchers have proposed the Hilbert Huang transform (HHT), which combines empirical mode decomposition (EMD) with HT [25]. The EMD algorithm is the core of the HHT algorithm, which can adaptively decompose the signals. However, the EMD algorithm is not suitable for signals with high-frequency content, which tends to lead to modal mixing [26]. Later, related researchers proposed ensemble empirical mode decomposition (EEMD), complementary ensemble empirical mode decomposition (CEEMD), complete ensemble empirical mode decomposition with adaptive noise (CEEMDAN), and other algorithms [27], [28], [29]. These algorithms perform a finite number of overall averages to the intrinsic mode functions (IMFs) to eliminate the interference of Gaussian white noise. However, this kind of method could make the interference elimination incomplete and affect the reconstructed signals. Furthermore, the decomposition results of these algorithms depend on the distribution of signal extremum points. In conclusion, these algorithms still tend to lead to modal mixing in the signal decomposition results.

Variational mode decomposition (VMD), as a new signal decomposition algorithm, can also be used to decompose the input signal into multiple IMFs [30]. From the mathematical derivation of the VMD, the VMD can be regarded as a group of adaptive optimal Wiener filters. The VMD algorithm is better in overcoming endpoint effects and modal mixing than recursive modal decomposition algorithms such as EMD and local mean decomposition (LMD). Therefore, the IMFs obtained from decomposing the motor vibration signal using the VMD algorithm are more suitable for HT. However, when applying the VMD algorithm for signal decomposition, it is crucial to appropriately configure the number of decomposition modes and the quadratic penalty factor. Fortunately, various optimization algorithms have been proposed by researchers to solve the above problem, such as the particle swarm optimization (PSO), the genetic algorithm (GA), the whale optimization algorithm (WOA), and other algorithms [31], [32], [33], [34], [35]. In general, these algorithms can find the optimal parameter combination for the VMD algorithm. However, these optimization algorithms can easily fall into local optimality.

The effectiveness of the VMD algorithm in decomposing the signal is mainly performed on whether there is modal mixing or over-decomposition in the obtained results. The relationship between its model parameter combination and the accuracy of the solution cannot be described by a specific expression, which exhibits black-box characteristics. Therefore, the only way to obtain the optimal parameter combination is to traverse all the discrete variable values. Finally, the parameter combination when there is almost no modal mixing and endpoint effects is regarded as the optimal parameter combination. Bayesian optimization is an efficient global optimization algorithm with high time efficiency and small evaluation cost, which has been widely used in deep learning hyperparameter tuning [36], [37]. Compared to other optimization algorithms, Bayesian optimization has a wider range of applications. Therefore, this study proposes to use Bayesian optimization to find the optimal parameter combination for the VMD algorithm, which further proposes an adaptive signal decomposition algorithm and applies it to the detection of ITSC in PMSM.

The main contributions of this study are as follows:
1) By introducing Bayesian optimization into the VMD, a Bayesian optimized adaptive parameter selection variational mode decomposition (BOAPS-VMD) nonlinear signal processing method is proposed, which overcomes the parameter selection problem of the VMD algorithm.
2) Combining the BOAPS-VMD with HT and applying it to the detection of ITSC in PMSM.
3) The cumulative variance contribution rate (C-VCR) is proposed to identify the fault signature components,

which further enhances the accuracy of fault detection. In addition, the presentation of results through 3D time-frequency diagrams enhances the representation of fault signatures.

4) The ability of BOAPS-VMD in different aspects is illustrated through simulation. In addition, real engineering case is applied to verify the effectiveness and engineering applicability of the proposed method.

The rest of this study is arranged as follows: In Section II, the basic principles of the BOAPS-VMD are introduced; Section III describes how to combine BOAPS-VMD with HT and apply it to the detection of ITSC in PMSM; Section IV analyzes the performance of the proposed BOAPS-VMD from different aspects through simulated signals; in Section V, an experimental platform for PMSM fault is established. The effectiveness and engineering applicability of the BOAPS-VMD are further verified with a practical engineering case. Section VI concludes the whole study.

II. ADAPTIVE PARAMETER SELECTION VARIATIONAL MODE DECOMPOSITION

A. VMD ALGORITHM
Decomposition of the signal using the VMD algorithm can obtain a series of mode functions that are described as amplitude-modulated-frequency-modulated (AM-FM) signals. The signals are described in detail in the [30]. The decomposition process of the VMD algorithm is mainly described as follows:

Assuming that the real-valued input signal is $f(t)$. $u_k(t)$ is the mode obtained by decomposition, each mode contains frequency components around the central frequency w_k. The HT is performed for the following mode:

$$\hat{u}_k(t) = u_k(t) * \frac{1}{\pi t} \tag{1}$$

further, the resolved signal $\tilde{u}_k(t)$ is obtained:

$$\tilde{u}_k(t) = u_k(t) + j\hat{u}_k(t) \tag{2}$$

After this, the resolved signal is multiplied by the exponential term $e^{-jw_k t}$ to obtain the baseband signal $S_k(t)$:

$$S_k(t) = \tilde{u}_k(t)e^{-jw_k t} \tag{3}$$

To estimate the bandwidth of the signal, the squared parametrization of the gradient is used. Meanwhile, to achieve separation of the signal, the following constrained variational problem is given:

$$\begin{cases} \min_{\{u_k\},\{w_k\}} \left\{ \sum_k \|\partial_t [S_k(t)]\|_2^2 \right\} \\ \text{s.t.} \sum_{k=1}^{k} u_k = f \end{cases} \tag{4}$$

where k is the set number of decomposition modes. $u_k = \{u_1, u_2, \ldots, u_k\}$, $w_k = \{w_1, w_2, \cdots, w_k\}$ are the IMFs and central frequencies obtained after decomposition of the input signal $f(t)$, respectively.

To find the optimal solution of the above equation (4), the quadratic penalty factor α and the Lagrange multiplier λ are introduced to construct the extended Lagrange equation, which transforms the above variational problem into an unconstrained variational problem:

$$\begin{aligned} L(&\{u_k\}, \{w_k\}, \lambda) \\ &= \alpha \sum_k \|\partial_t [S_k(t)]\|_2^2 \\ &+ \left\| f(t) - \sum_k u_k(t) \right\|_2^2 + \left\langle \lambda(t), f(t) - \sum_k u_k(t) \right\rangle \end{aligned} \tag{5}$$

In this case, the alternating direction method of multipliers (ADMM) combined with Perceval's theorem is used to optimize the modes $u_k(t)$, the central frequency w_k, and the Lagrange multiplier λ. In this process, $u_k(t)$, w_k, and λ are updated with the following equations:

$$\hat{u}_k^{n+1}(w) = \frac{\hat{f}(w) - \sum_{i \neq k} \hat{u}_i(w) + \frac{\hat{\lambda}(w)}{2}}{1 + 2\alpha(w - w_k)^2} \tag{6}$$

$$w_k^{n+1} = \frac{\int_0^\infty w|\hat{u}(w)|^2 dw}{\int_0^\infty |\hat{u}(w)|^2 dw} \tag{7}$$

$$\hat{\lambda}^{n+1}(w) = \hat{\lambda}^n(w) + \tau\left(\hat{f}(w) - \sum_k \hat{u}_k^{n+1}(w)\right) \tag{8}$$

where τ is the time step and n is the number of iterations.

The ADMM algorithm converges when the following condition is met:

$$\sum_k \left\| \hat{u}_k^{n+1} - \hat{u}_k^n \right\|_2^2 / \left\| \hat{u}_k^n \right\|_2^2 < \xi \tag{9}$$

where ξ is the convergence error and usually takes the value 1×10^{-7}.

According to the above theory, setting different parameter combination $[k, \alpha]$ will give different computational results.

B. BAYESIAN OPTIMIZATION
Bayesian optimization is primarily based on Bayes' theorem, which fits the true objective function with a probabilistic iterative model. Finally, the most likely subsequent points are evaluated based on the results of the fit [38]. In this process, Bayesian optimization uses existing information to reduce the number of evaluations and improve the efficiency of the calculation. When using Bayesian optimization, a reasonable probabilistic agent model and acquisition function should be chosen to obtain better optimization results.

1) PROBABILISTIC AGENT MODEL
The Gaussian process in the non-parametric model is more widely used, more flexible, and less prone to "over-fitting". This study uses the Gaussian process as a probabilistic agent model in Bayesian optimization. The mathematical

expressions are as follows:

$$\begin{cases} \varphi(x) \sim GP\left[m(x), k\left(x, x'\right)\right] \\ m(x) = E[\varphi(x)] \\ k\left(x, x'\right) = E\left\{[\varphi(x) - m(x)]\left[\varphi\left(x'\right) - m\left(x'\right)\right]\right\} \end{cases} \quad (10)$$

In the above equations, φ is the unknown function, $m(x)$ is the mean function, and $k\left(x, x'\right)$ is the positive semi-definite covariance function. In the Gaussian process, a finite number of random variables all satisfy a Gaussian joint distribution. Suppose there exists a prior distribution with a mean of 0:

$$p(\psi \mid X, \theta) = N(0, \Sigma) \quad (11)$$

where X represents the training set; ψ represents the set of function values of the unknown function φ; Σ represents the covariance matrix composed of $k\left(x, x'\right)$; and θ represents the hyperparameters.

Assuming that there exists noise ε satisfying an independent identically distributed Gaussian distribution $p(\varepsilon) = N\left(0, \sigma^2\right)$, the likelihood distribution is obtained:

$$p(Y \mid \psi) = N\left(\psi, \sigma^2 \boldsymbol{I}\right) \quad (12)$$

The joint distribution exists:

$$\begin{bmatrix} Y \\ \psi_* \end{bmatrix} \sim N\left(0, \begin{bmatrix} \Sigma + \sigma^2 \boldsymbol{I} & K_* \\ K_*^T & K_{**} \end{bmatrix}\right) \quad (13)$$

$$K_*^T = \{k\left(x_1, X_*\right), k\left(x_2, X_*\right), \cdots, k\left(x_t, X_*\right)\} \quad (14)$$

$$K_{**} = k\left(X_*, X_*\right) \quad (15)$$

where ψ_* represents the prediction function value and X_* is the prediction input. Finally, the prediction distribution is obtained as follows:

$$\begin{cases} p\left(\psi_* \mid X, Y, X_*\right) = N\left(\langle\psi_*\rangle, \text{cov}\left(\psi_*\right)\right) \\ \langle\psi_*\rangle = K_*^T \left[\Sigma + \sigma^2 \boldsymbol{I}\right]^{-1} Y \\ \text{cov}\left(\psi_*\right) = K_{**} - K_*^T \left[\Sigma + \sigma^2 \boldsymbol{I}\right]^{-1} K_* \end{cases} \quad (16)$$

where $\langle\psi_*\rangle$ represents the predicted mean; $\text{cov}\left(\psi_*\right)$ represents the predicted covariance.

2) ACQUISITION FUNCTION

In the Bayesian optimization, the expected improvement (EI) strategy has the advantage of fewer parameters. Therefore, this study uses the EI strategy as the acquisition function for Bayesian optimization:

$$\gamma = \phi\left(\frac{v^* - \mu_t(x)}{\sigma_t(x)}\right) \quad (17)$$

$$\alpha_t\left(x; D_{1:t}\right) = \begin{cases} \left[v^* - \mu_t(x)\right]\gamma + \sigma_t(x)\gamma, & \sigma_t(x) > 0 \\ 0, & \sigma_t(x) = 0 \end{cases} \quad (18)$$

where v^* represents the current optimal objective function value; ϕ represents the standard normal distribution cumulative density function.

C. BAYESIAN OPTIMIZED VARIATIONAL MODE DECOMPOSITION

This study uses Bayesian optimization to find the optimal parameter combination for the VMD algorithm and proposes a Bayesian optimized adaptive parameter selection variational mode decomposition (BOAPS-VMD) nonlinear signal processing method. When using Bayesian optimization to find the optimal parameter combination, the evaluation function needs to be given. The selection of the evaluation function determines the effectiveness of the Bayesian optimization and the accuracy of the final decomposition of the signal. In response, the following analysis is carried out:

When the PMSM is in actual operation, the vibration signal is more susceptible to interference from external factors. Therefore, after the vibration signal of the PMSM is decomposed by the VMD algorithm, the resulting IMFs contain more concentrated frequency components and are more prone to modal mixing. From the previous theory, it is clear that after decomposing the real-valued input signal, each IMF contains different central frequencies. If modal mixing occurs, the frequencies of different IMFs will be superimposed on each other. The Hilbert envelope spectrum can better characterize the spectrum of the nonlinear signal compared to the FFT. It is now widely used for fault detection [39]. In addition, the information entropy can describe the information content of the signal. Therefore, this study proposes to use envelope entropy to describe the frequency components contained in each IMF and uses it to construct the evaluation function for Bayesian optimization.

Assume that $u_i(n)$ is the *ith* IMF obtained after the VMD decomposition of the input signal, which is transformed by the HT to obtain the resolved signal $\tilde{u}_i(n)$. After this, Hilbert demodulation is performed to obtain the envelope signal sequence $Z_i(n)$:

$$Z_i(n) = \sqrt{u_i(n)^2 + \tilde{u}_i(n)^2} \quad (19)$$

where n is the signal sampling point. The probability distribution p_i of the signal sequence is calculated:

$$p_i = Z_i(n) / \sum_{n=1}^{N} Z_i(n) \quad (20)$$

where N is the total number of sampling points of the signal. Finally, the envelope entropy E_s is obtained according to the definition of Shannon's entropy:

$$E_s = -\sum_{i=1}^{N} p_i \log_2 p_i \quad (21)$$

In practical engineering applications, the single use of envelope entropy as the evaluation function for Bayesian optimization can easily lead to over-decomposition in the VMD algorithm, making the decomposed mode a simple harmonic. Kurtosis is a dimensionless parameter that describes the steepness of the waveform distribution and is proportional to the number of shock components in the signal [40]. It also

reflects the energy of the signal. Therefore, to better characterize the vibration signal of PMSM, the kurtosis is further introduced into the construction of the evaluation function.

The method for calculating the kurtosis value K_s of the IMF obtained from the VMD decomposition is as follows:

$$K_s = \frac{1}{N} \sum_{n=1}^{N} u(n)^4 \qquad (22)$$

Combining the above analysis, the resulting Bayesian optimization evaluation function $EvaF$ is constructed as:

$$EvaF = \frac{1}{k} \sum_{i=1}^{k} \left(\lambda \cdot E_s + \gamma \cdot \frac{1}{K_s} \right) \qquad (23)$$

where k is the number of IMFs obtained from the decomposition, λ is the weight factor of envelope entropy, γ is the weight factor of kurtosis, $\lambda + \gamma = 1$. In this study, the sensitivity of the envelope entropy and the kurtosis to the decomposition results of the vibration signal is relatively close, therefore, set $\lambda = \gamma = 0.5$. Finally, using Bayesian optimization to find the optimal parameter combination for the VMD algorithm can be equated to solving the following equation:

$$x^* = \arg \min \ EvaF(x), \quad x \in X \qquad (24)$$

where x denotes a set of parameter combination; X is the parameter combination space; x^* is a set x in the combination space that the objective function achieves an optimal solution.

This study uses the Gaussian process to proxy the black-box objective function relationship between different parameter combinations and the VMD model. Afterwards, the posterior distribution is obtained from the observed dataset. At the same time, the next evaluation point is selected using the EI acquisition function to iteratively correct the prior information and continuously improve the accuracy of the agent model. Finally, the optimal parameter combination is obtained. The main optimization process for the VMD algorithm is given in Fig. 1.

III. PMSM FAULT DETECTION TECHNIQUE
To detect the ITSC in PMSM, the proposed BOAPS-VMD signal processing method is combined with HT. The detailed steps for fault detection are as follows:

1) The motor vibration signal is collected using the vibration sensor.
2) The collected 1D time series are input into the VMD.
3) Parameter combination optimization is implemented for VMD by using Bayesian optimization according to Fig. 1. The evaluation function in the optimization process is a real functional relationship between the performance of the VMD model and the parameter combination. In this process, the acquisition function is used at each iteration to obtain the parameter combination for VMD to decompose the input signal. The parameter combination that makes the convergence accuracy as high as possible will be selected. Firstly, the parameters to be optimized are specified, such as the
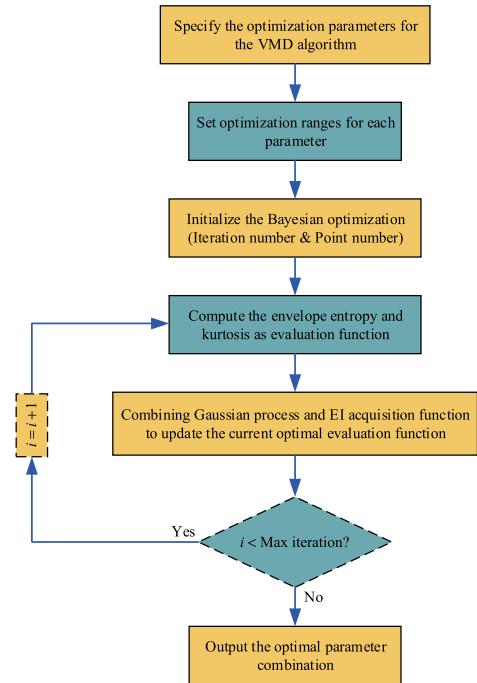

FIGURE 1. Optimization process for the VMD algorithm using Bayesian optimization.

number of decomposition modes k and the quadratic penalty factor α of the VMD. Secondly, the optimization ranges are set for each parameter. After that, the Bayesian optimization loop is performed according to the evaluation function of Eq. (23). In this process, the Gaussian process is utilized to model the functional relationship between VMD performance and the parameter combination. Furthermore, the EI acquisition function is used to guide the subsequent sampling. Finally, the optimal parameter combination $[k, \alpha]$ for the VMD is obtained.

4) The optimal parameter combination $[k, \alpha]$ is combined with VMD to decompose the input signal to obtain k IMFs.
5) The IMFs are further analyzed using C-VCR and HT to complete the fault detection.

Assuming that the ith IMF obtained from the decomposition is $u_i(t)$. Calculating its variance contribution rate (VCR), which is marked as $Contr_i$:

$$Contr_i = \left\{ D\left[u_i(t)\right] / \sum_{i=1}^{k} D\left[u_i(t)\right] \right\} \times 100\% \qquad (25)$$

where $D[\cdot]$ represents the variance of the signal. The VCRs for each IMF are then sorted from largest to smallest. For the first $j[j = 1, 2, \cdots, l \ (l \le k)]$ VCRs after sorting, C-VCR can be obtained by adding them up, denoted as $Cvcr_j$ [41]. The expression is:

$$Cvcr_j = \sum_{i=1}^{j} Contr_i \qquad (26)$$

Finally, a threshold *CL* is set such that when Eq. (27) is satisfied, the number of IMFs containing fault signature information can be identified. That is, the first *l* IMFs with VCRs sorted from largest to smallest. In this study, the threshold *CL* for C-VCR is set to 90%.

$$Cvcr_j \geq CL \tag{27}$$

Suppose $\eta(t)$ is an IMF identified by the C-VCR:

$$\hat{\eta}(t) = H[\eta(t)] = \frac{1}{\pi} \int_{-\infty}^{+\infty} \frac{\eta(\tau)}{t - \tau} d\tau \tag{28}$$

where $H[\cdot]$ denotes the Hilbert function transformation of $\eta(t)$. Construct the resolved signal $\tilde{\eta}(t)$:

$$\tilde{\eta}(t) = \eta(t) + j\hat{\eta}(t) \tag{29}$$

$$\begin{cases} a(t) = \sqrt{\eta^2(t) + \hat{\eta}^2(t)} \\ \theta(t) = \arctan\left[\dfrac{\hat{\eta}(t)}{\eta(t)}\right] \end{cases} \tag{30}$$

where $a(t)$ is the instantaneous amplitude function, $\theta(t)$ is the instantaneous phase function. The instantaneous frequency function $\varepsilon(t)$ of the signal is further obtained:

$$\varepsilon(t) = \frac{1}{2\pi}\delta(t) = \frac{1}{2\pi}\frac{d\theta(t)}{dt} \tag{31}$$

where $\delta(t)$ is the instantaneous angular frequency. The Hilbert spectrum is obtained as follows:

$$H(\delta, t) = \text{Re}\left[a(t)e^{j\int \delta(t)dt}\right] \tag{32}$$

Define $E(\delta, t)$ as the distribution of signal energy in the frequency and time planes, which in turn defines the 3D time-frequency diagram:

$$E(\delta, t) = \left\{\text{Re}\left[a(t)e^{j\int \delta(t)dt}\right]\right\}^2 \tag{33}$$

The main implementation process for fault detection is shown in Fig. 2.

IV. SIMULATION AND RESULTS ANALYSIS
A. SIMULATION MODEL BUILDING
A two-dimensional finite element simulation model for ITSC in PMSM is established in ANSYS Electronics Desktop software. The theory of finite element modeling is described in detail in [42]. The basic parameters of the PMSM are shown in TABLE 1, its power supply is inverter powered and the control of the inverter is SPWM.

To analyze the ITSC in PMSM, a simulation circuit for a short circuit is given in Fig. 3, with switch S1 initially in the open position. This study assumes that the motor starts at the moment t = 0. After a while, the motor enters a stable operation state. Then, S1 is closed, at which point there is a part of the faulty winding (W_Asc) is short-circuited out of phase A. W_B and W_C represent the B and C phase windings, while W_An denotes the remaining normal winding in phase A. R_{Az}, R_{As}, R_{Bw}, and R_{Cw} represent the winding resistances, while L_{Az}, L_{Bw}, and L_{Cw} denote the winding inductances. The
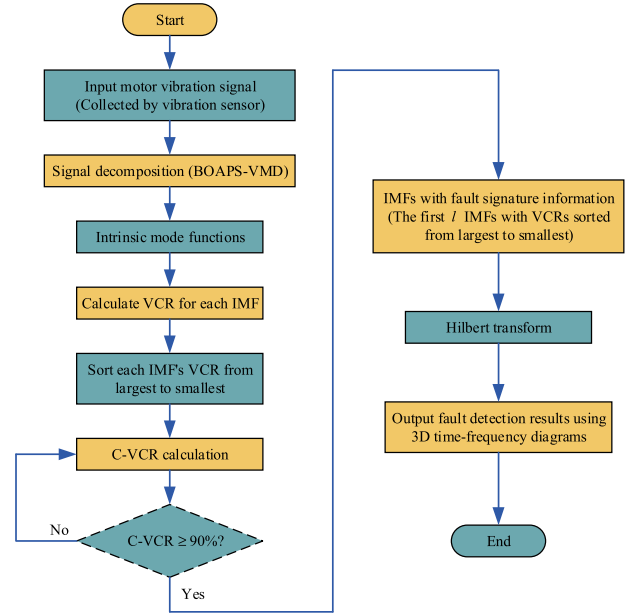

FIGURE 2. Implementation process for fault detection in PMSM.

TABLE 1. Basic parameters of the finite element model.

Parameter	Numerical value
Rated power (kW)	1.33
Frequency (Hz)	50
Rated voltage (V)	330
Rated speed (rpm)	200
Polar logarithm	15
Stator O.D. (mm)	247
Rotor O.D. (mm)	160.7
Number of stator slots	27

normal winding and the faulty winding are in series before the short circuit. After the short circuit occurs, both ends of the faulty winding are shorted. R_{ex} is the contact resistance.

Fig. 4 shows the finite element solution model combining the basic parameters and the equivalent circuit. The stator and rotor cores of the motor are specified as DW465-50 material, and the stator winding is made of pure copper with a conductivity of 58,000,000 S/m. The material of the permanent magnet is set as NdFe35 [43], [44]. For the rest of the solution area, the eddy current losses are ignored, and the permeability and conductivity are set to vacuum.

B. GRID SECTIONING
To analyze the spatial variation of the field with high accuracy, the finite element grid must be sufficiently detailed. However, the problem is that the solution time increases and the memory consumption increases. Considering the small rotating air gap of the PMSM, the magnetic field changes in the rotating air gap and stator tooth slot part are more complicated [45]. To improve the accuracy of the solution as much as possible, this study uses small grids for this part.
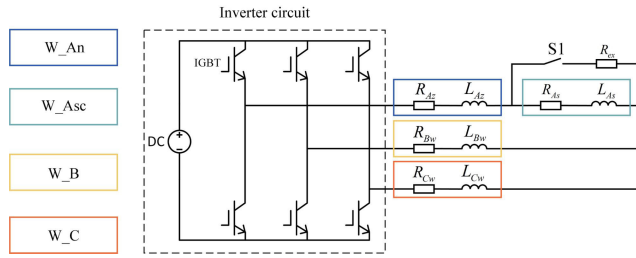
FIGURE 3. Simulation circuit for a short circuit.
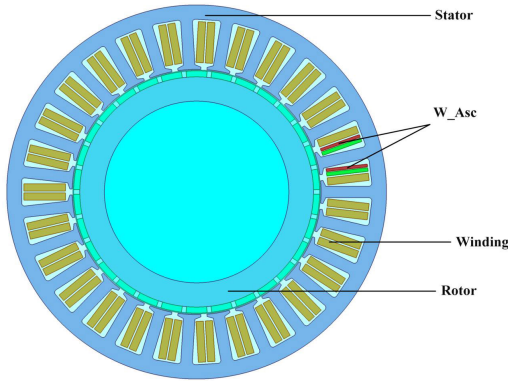

FIGURE 4. Two-dimensional finite element simulation model for ITSC in PMSM.

At the same time, to save solution time, large grids are used for the more regularly shaped parts such as the stator and rotor. Fig. 5 shows the results of the grid sectioning.
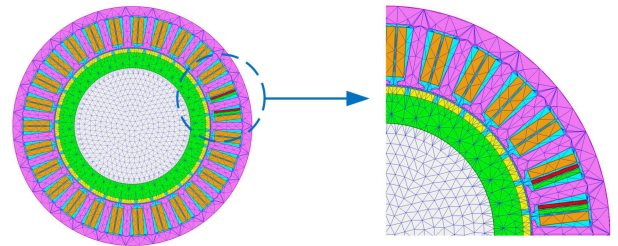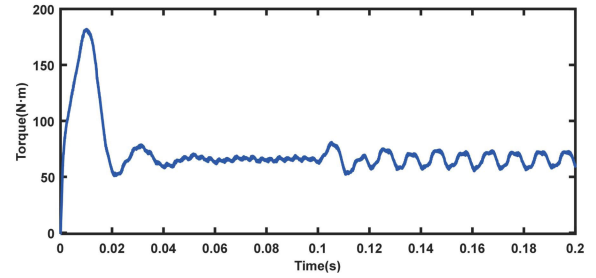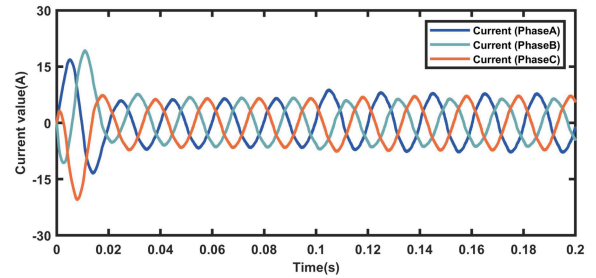
C. FINITE ELEMENT SOLUTION PARAMETER SETTING
The model of the motor is solved using the field-circuit coupled time-domain finite element method [46], [47]. As the motor takes time to transition from start-up to stable running condition. The solution time and step should be set appropriately. After analysis, 0.02s is one cycle time of the rated frequency 50Hz. To guarantee the solution accuracy, the solver is configured to solve at t =0s, with a solution step of 0.0002s. The moment of short circuit is 0.1s, and the total solution time is 0.2s.

D. SIMULATION RESULTS
After solving, Fig. 6 shows the solved motor torque signal and the three-phase current signal. It can be seen from Fig. 6 that after the motor is started from t =0s, the torque and three-phase current are initially unstable. After a while, the two signals gradually stabilize, with the torque signal showing fluctuating characteristics. In addition, the torque and three-phase currents change abruptly after the motor fault, the torque fluctuation increases in intensity and the three-phase currents are no longer balanced. The results verify the validity of the simulation model and the accuracy of the solution parameter setting.

E. ANALYSIS OF SIMULATION RESULTS
The torque signal in the finite element simulation is sampled at 160 kHz. Torque fluctuation is a constant instability

FIGURE 5. Grid sectioning results.

(a) Motor torque signal

(b) Motor three-phase current signal

FIGURE 6. Finite element simulation results.

characteristic of the PMSM and can lead to negative effects such as motor vibration and noise. The torque fluctuation signal of the PMSM is similar to the vibration signal in that both are nonlinear signals. In this section, a nonlinear signal (torque fluctuation signal) during motor operation is analyzed using the proposed BOAPS-VMD.

Firstly, to observe the frequency changes in the torque fluctuation signal after the motor fault, the torque fluctuation signal from 0.05s to 0.1s before the motor fault and the torque fluctuation signal from 0.15s to 0.2s after the motor fault is analyzed using FFT respectively. Fig. 7 shows the torque fluctuation signals obtained after amplitude normalization for the two time periods. Fig. 8 shows the spectrograms corresponding to the two signals.

Analysis of Fig. 8 shows that the 100 Hz frequency (2x rotation frequency) is the main frequency that appears in the torque fluctuation signal after the motor fault. This result shows that the 2x rotation frequency is the main fault signature frequency in the motor torque fluctuation signal. Following this, the BOAPS-VMD is used to analyze the torque fluctuation signal from 0.15s to 0.2s shown in Fig. 7(b).
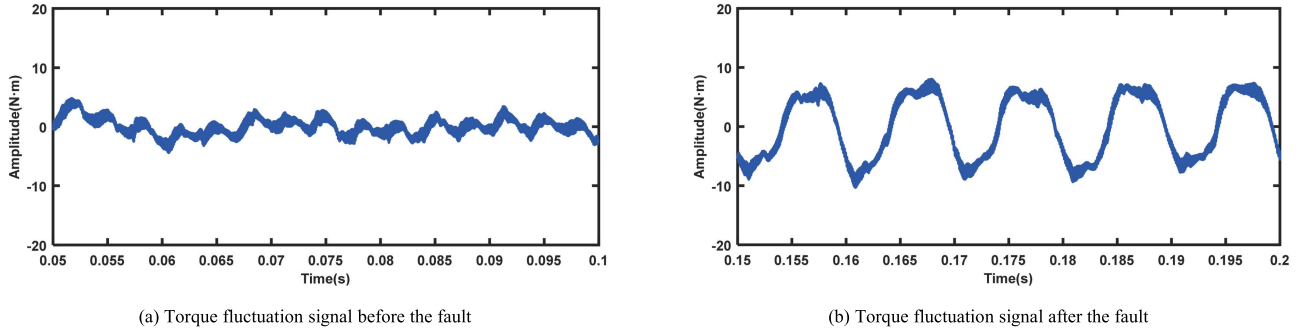
(a) Torque fluctuation signal before the fault

(b) Torque fluctuation signal after the fault

FIGURE 7. Torque fluctuation signals after amplitude normalization.

(a) Spectrogram of torque fluctuation signal before the fault

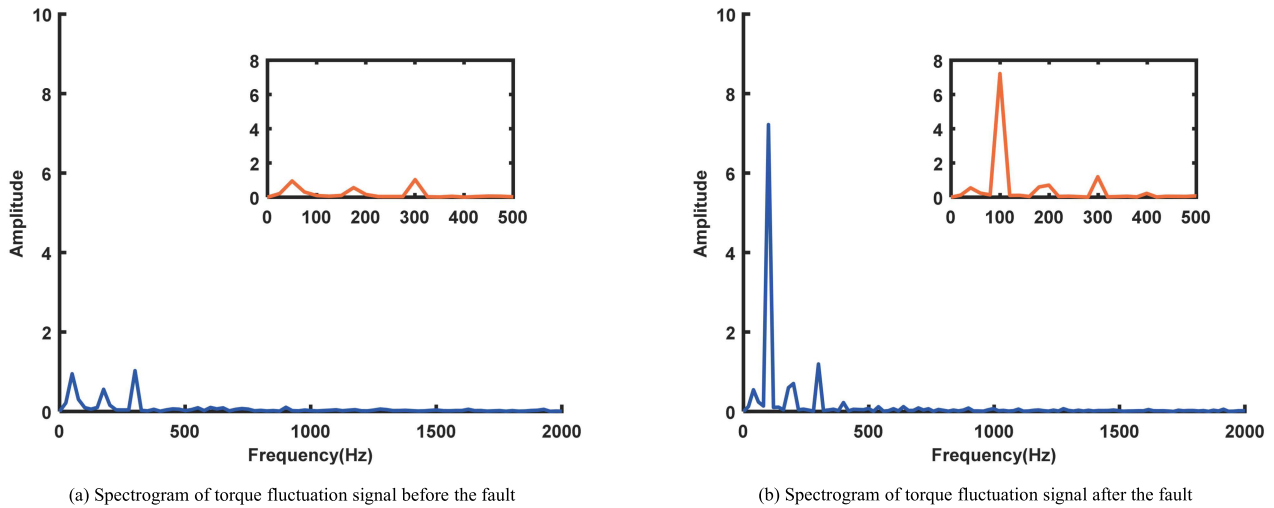(b) Spectrogram of torque fluctuation signal after the fault

FIGURE 8. Spectrograms of torque fluctuation signals.

It is worth noting that when using Bayesian optimization to find the optimal parameter combination $[k, \alpha]$, the optimization ranges for two parameters need to be specified in advance. From the above theory, it is clear that the decomposition mode number k is related to the spectral characteristics and decomposition accuracy of the signal. The quadratic penalty factor α is related to the frequency characteristics of the signal. Combining references and experimental experience, this study suggests the following method for determining the optimization ranges of the parameters:

1. To determine the optimization range of the decomposed mode number k, the EMD algorithm is used to decompose the signal, and the number of IMFs obtained is recorded as K_0. Finally, the optimization range of k is chosen as $[K_0/2, 2K_0]$.

2. Set the value of the initial quadratic penalty factor α to the Nyquist sampling frequency f_0 of the signal, and choose the optimization range of the quadratic penalty factor α to be $[f_0, 10f_0]$.

Based on the above analysis, the signal is first decomposed using the EMD algorithm to obtain 8 IMFs, thus the optimal range for the decomposition mode number k is specified as $[4, 16]$. In combination with the sampling frequency of

the torque fluctuation signal, the optimization range for α is specified as $[80000, 800000]$.

After this, the Bayesian optimization is performed. Three independent repeat tests are carried out and the parameters set in each optimization are shown in TABLE 2. After several iterations of the test, it is found that the minimum value of the evaluation function converges to 1.49. The processes of Bayesian optimization are shown in Fig. 9. The convergence curves for Bayesian optimization are given in Fig. 10. The results of the parameter combination $[k, \alpha]$ obtained from the three optimizations are shown in TABLE 3.

The three optimization results are averaged to obtain the optimal parameter combination. Finally, the optimal parameter combination obtained by Bayesian optimization is [10, 3.18947E+05]. The VMD algorithm is used to decompose the torque fluctuation signal in combination with this parameter combination. The 10 IMFs obtained from the BOAPS-VMD decomposition and the corresponding spectrograms for each IMF are given in Fig. 11.

After this, the VCR and the C-VCR for each IMF are calculated and the results are shown in Fig. 12. In this study, the threshold of C-VCR is set to 90%, which means that

TABLE 2. Bayesian optimization parameters setting.

Test	MaxObjectiveEvaluations (Iterations)	NumSeedPoints (Points)
1	100	10
2	100	20
3	100	30

(a) Bayesian optimization process for the 1st test

(b) Bayesian optimization process for the 2nd test
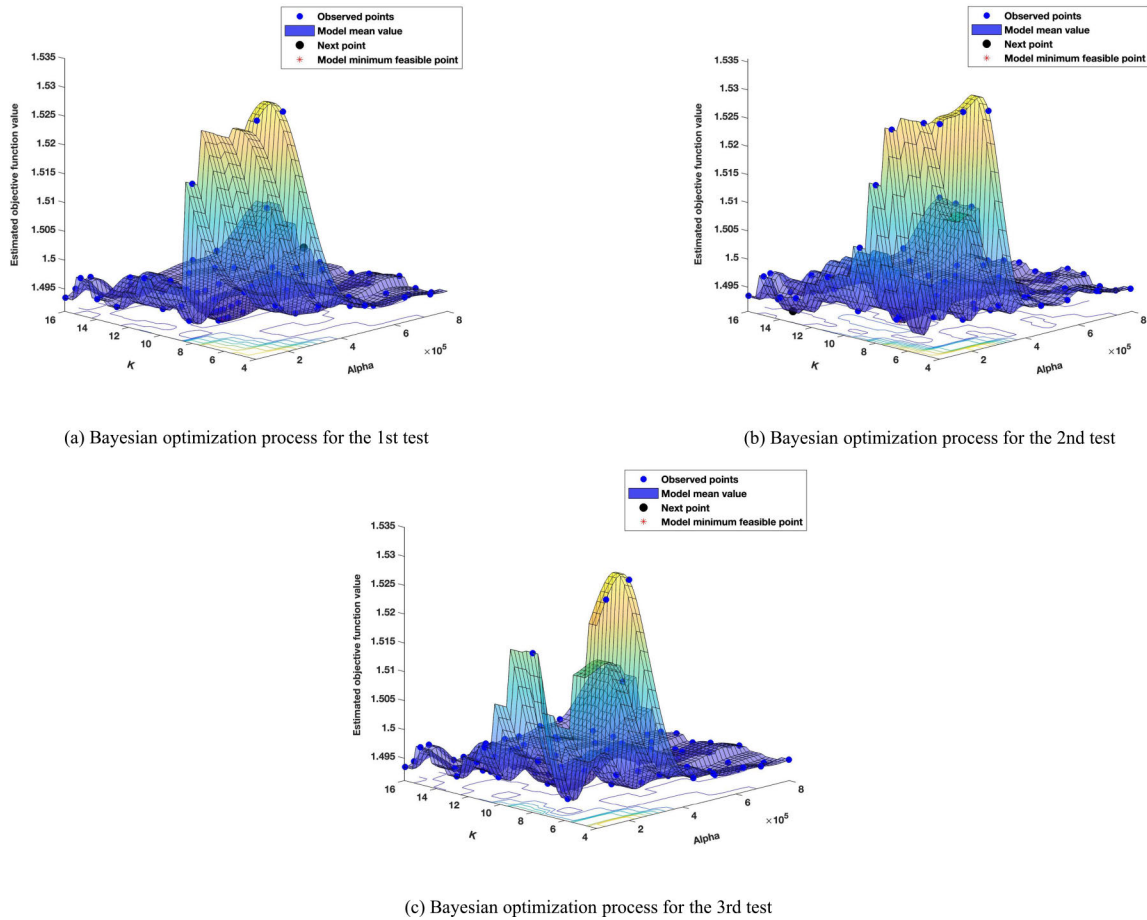
(c) Bayesian optimization process for the 3rd test

FIGURE 9. The processes of Bayesian optimization for torque fluctuation signal.
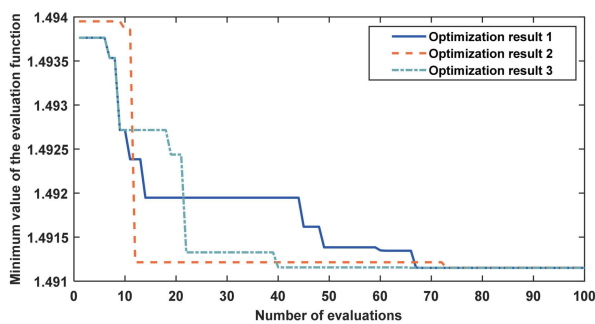
FIGURE 10. Bayesian optimization convergence curves for torque fluctuation signal.

the first several IMFs with a C-VCR of 90% are selected as the fault signature components. From Fig. 12, it can be seen that a single IMF is sufficient to satisfy the requirement of 90% C-VCR. Therefore, the component which contains the

fault signature information is IMF9. Afterwards, the IMF9 is further analyzed. Meanwhile, to further analyze the adaptive properties of the BOAPS-VMD algorithm, a comparison is given. Two different parameter combinations are set up in the comparison, the first one is $k = 8, \alpha = 3.18947\text{E} + 05$; the second one is $k = 10, \alpha = 100000$. Afterwards, the torque fluctuation signal is decomposed respectively using these two sets of parameter combination combined with the VMD algorithm. Finally, the spectrograms containing the fault signature frequency are given in Fig. 13. Through observation of Fig. 13, there is an unavoidable phenomenon of modal mixing in the results obtained from other parameter combinations. A comprehensive analysis of Fig. 8 and Fig. 13 shows that the C-VCR performs well in identifying the fault signature frequency, which improves the accuracy of fault detection.

It is worth noting that, this comparison also shows that unreasonable setting of parameter combination can affect the

TABLE 3. The results of bayesian optimization.

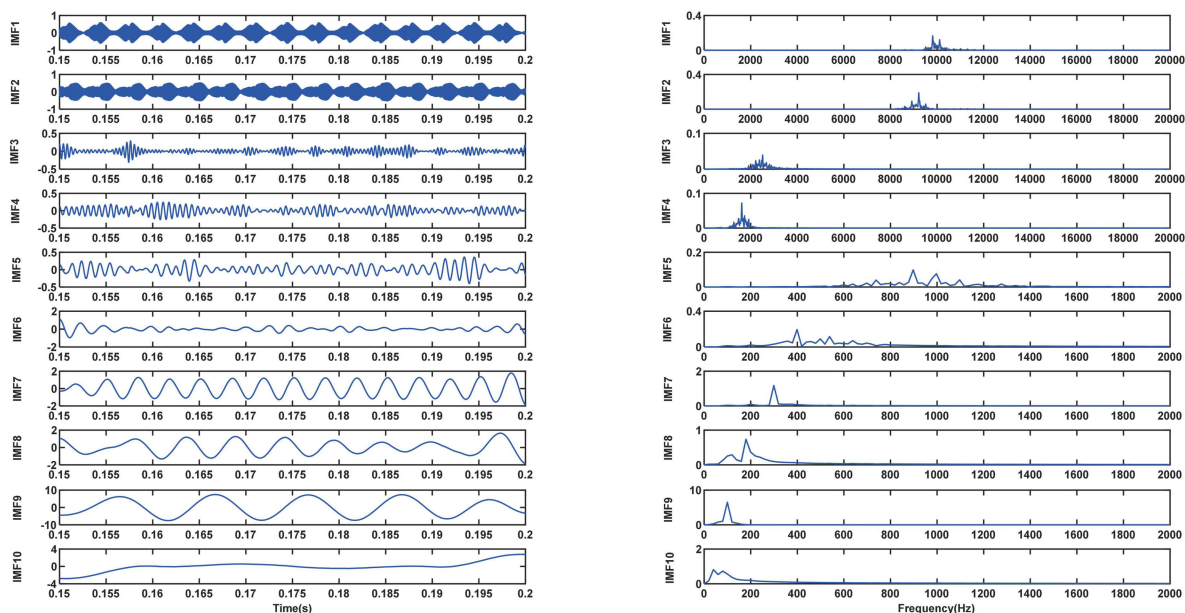| Test	K	Alpha
1	10	3.1245E+05
2	10	3.1385E+05
3	10	3.3054E+05

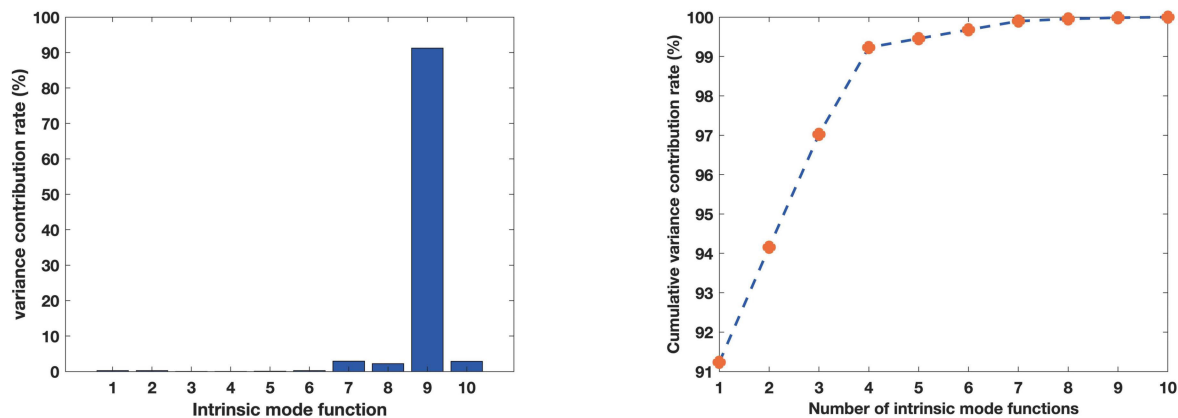**FIGURE 11.** Results of BOAPS-VMD decomposition for torque fluctuation signal.

FIGURE 12. Calculation results of VCR and C-VCR for each IMF (Left: VCR; Right: C-VCR).

effectiveness of signal decomposition, which further demonstrates the adaptive properties of the BOAPS-VMD.

To further evaluate the effectiveness and accuracy of the BOAPS-VMD, the torque fluctuation signal is decomposed using the EEMD, CEEMD, CEEMDAN, and WPT algorithms respectively.

When using the WPT algorithm to decompose the signal, the basis function is specified as the db8 wavelet, and

the number of decomposition layers is set to 10. After the algorithms are solved, both EEMD and CEEMD algorithms obtain 12 IMFs. The CEEMDAN algorithm obtains 15 IMFs and the WPT algorithm obtains 1024 wavelet packet coefficients in layer 10. Fig. 14 gives the calculation results of VCR and C-VCR for each component under different algorithms (The CEEMDAN algorithm and the WPT algorithm only show the calculation results for the first 12 components).
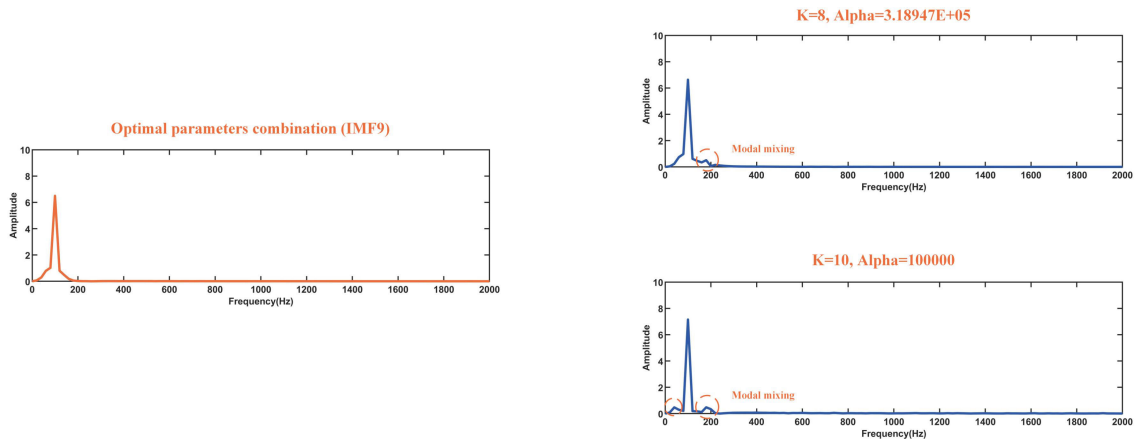
FIGURE 13. Spectrograms of fault signature frequency obtained from the VMD algorithm under different parameter combinations.
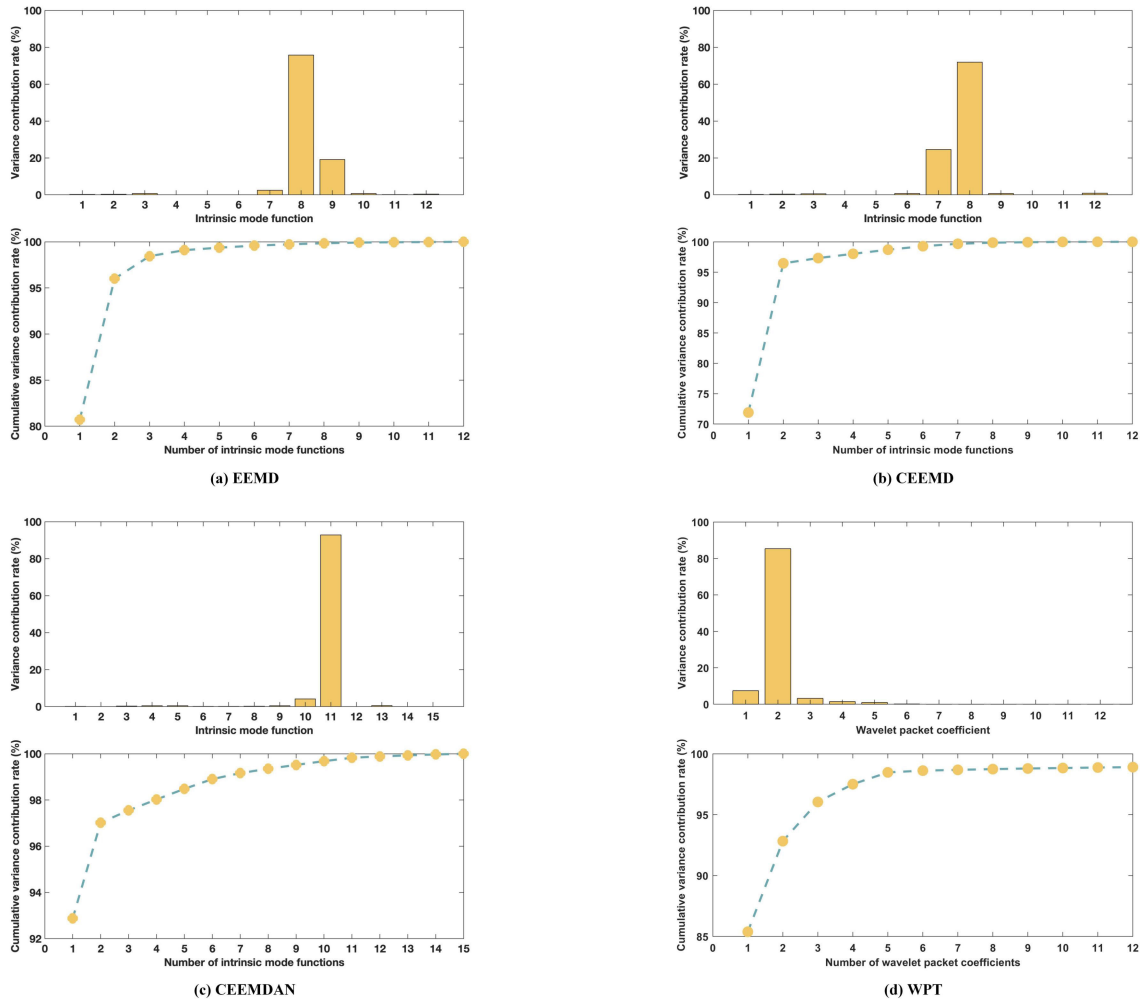

FIGURE 14. Calculation results of VCR and C-VCR for each component under different algorithms.

As can be seen in Fig. 14, the EEMD, CEEMD, and WPT algorithms combined with C-VCR all require two components to meet the 90% C-VCR requirement. In addition, nents to meet the 90% C-VCR requirement. In addition,

Fig. 14 shows that in the decomposition results of the EEMD algorithm, the fault signature components are IMF8 and IMF9; in the decomposition results of the CEEMD algorithm,
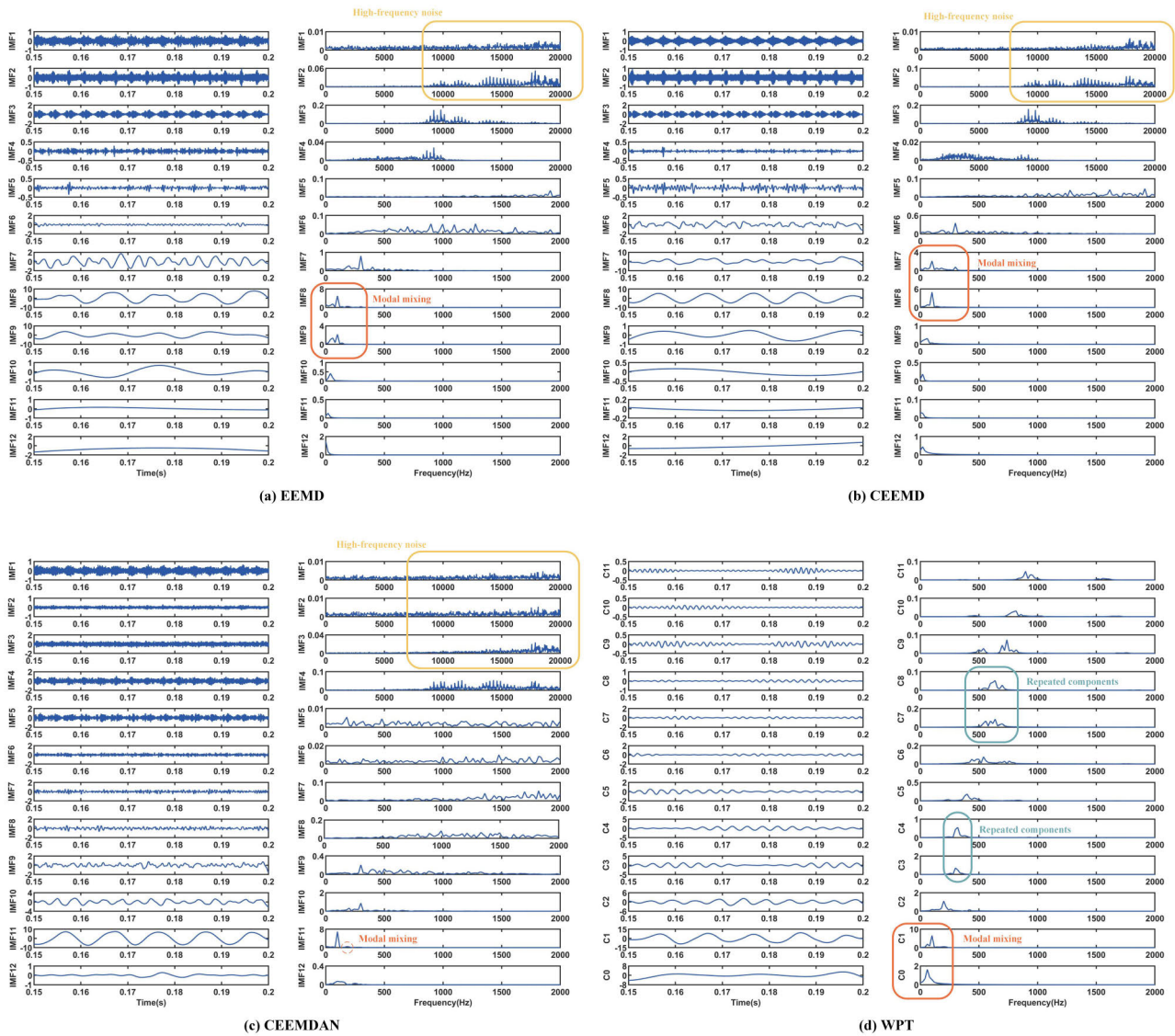
FIGURE 15. Decomposition results for the EEMD, CEEMD, CEEMDAN and WPT algorithms.

the fault signature components are IMF7 and IMF8; in the decomposition results of the CEEMDAN algorithm, the fault signature component is IMF11; and in the decomposition results of the WPT algorithm, the fault signature components are wavelet packet coefficients 1 and 2.

The first 12 IMFs from the EEMD, CEEMD, and CEEM-DAN algorithm decomposition results and the first 12 wavelet packet coefficients from layer 10 of the WPT algorithm decomposition results are given in Fig. 15. In addition, the spectrograms of each component are given in Fig. 15. Through observation of Fig. 15, the EEMD, CEEMD, and CEEMDAN algorithms all show significant modal mixing in decomposition results, which causes strong interference in the identification of the fault signature components. As can be seen in Fig. 15(d), the WPT algorithm can analyze the full frequency band of the signal compared to the EEMD,

CEEMD, and CEEMDAN algorithms and can better separate the fault signature components. However, the WPT algorithm needs to consider the decomposition scale and the selection of the basis function based on the input signal, which lacks adaptive properties. It is worth noting that the decomposition processes of the EEMD, CEEMD, and CEEMDAN algorithms all introduce Gaussian white noise. The decomposition results show that the white noise is not eliminated, which also causes some interference in the identification of the fault signature frequency. Compared to other algorithms, it can be seen that the BOAPS-VMD can better separate the fault signature component. Meanwhile, compared to other algorithms, the BOAPS-VMD is more robust to noise, and can further reduce interference from extraneous frequencies, which is more accurate in the decomposition of the signal and is more adaptive.

F. NOISE ROBUSTNESS ANALYSIS

In order to verify the noise robustness of the proposed BOAPS-VMD, a noise robustness test is conducted. In this study, multiple Gaussian white noises are systematically introduced to the torque fluctuation signal (original signal) shown in Fig. 7(b). In order to evaluate the performance of the BOAPS-VMD under different signal to noise ratio (SNR) conditions, the noise-added signals are decomposed using the BOAPS-VMD, EEMD, CEEMD, CEEMDAN, and WPT respectively. After that, the components identified by C-VCR (threshold set to 90%) are reconstructed to get the reconstructed signal. In this study, three metrics are considered: signal to noise ratio (SNR), normalized correlation coefficient (NCC), and mean square error (MSE). These metrics are used to fully evaluate the processing performance of the algorithms in noisy environments. Their mathematical expressions are as follows:

$$SNR = 10 \lg \frac{\sum_{i=1}^{N} x_i^2}{\sum_{i=1}^{N} [y_i - x_i]^2} \quad (34)$$

$$NCC = \frac{\sum_{i=1}^{N} x_i \cdot y_i}{\sqrt{(\sum_{i=1}^{N} x_i^2) \cdot (\sum_{i=1}^{N} y_i^2)}} \quad (35)$$

$$MSE = \frac{1}{N} \sum_{i=1}^{N} |x_i - y_i|^2 \quad (36)$$

where x_i is the sample point of the original signal, y_i is the sample point of the reconstructed signal and N is the length of the signal.

In presenting the computational results of SNR, NCC, and MSE, the noise standard deviation is used as the horizontal coordinate in order to more directly observe the performance of each algorithm under different noise levels. The standard deviation of the noise is a visual metric of the noise level, with a larger standard deviation of the noise indicating a greater intensity of the noise, and a smaller standard deviation of the noise indicating a weaker noise. For example, if the SNR of noise-added signal is −8dB, the standard deviation of the noise is 13.2533. Fig. 16 gives the calculation results of SNR, NCC, MSE for the original signal, reconstructed signals under different algorithms with different noise standard deviation.

As can be seen in Fig. 16(a), the SNR of the signal usually decreases as the standard deviation of the noise increases. Compared to the other algorithms, the BOAPS-VMD shows the best SNR performance, and the SNR is almost always larger than 0. Fig. 16(b) shows the NCC results of each algorithm under different noise standard deviations. NCC is a metric used to measure the similarity of two signals. The closer the NCC value is to 1, the more similar the two signals are. From Fig. 16(b), it can be seen that the
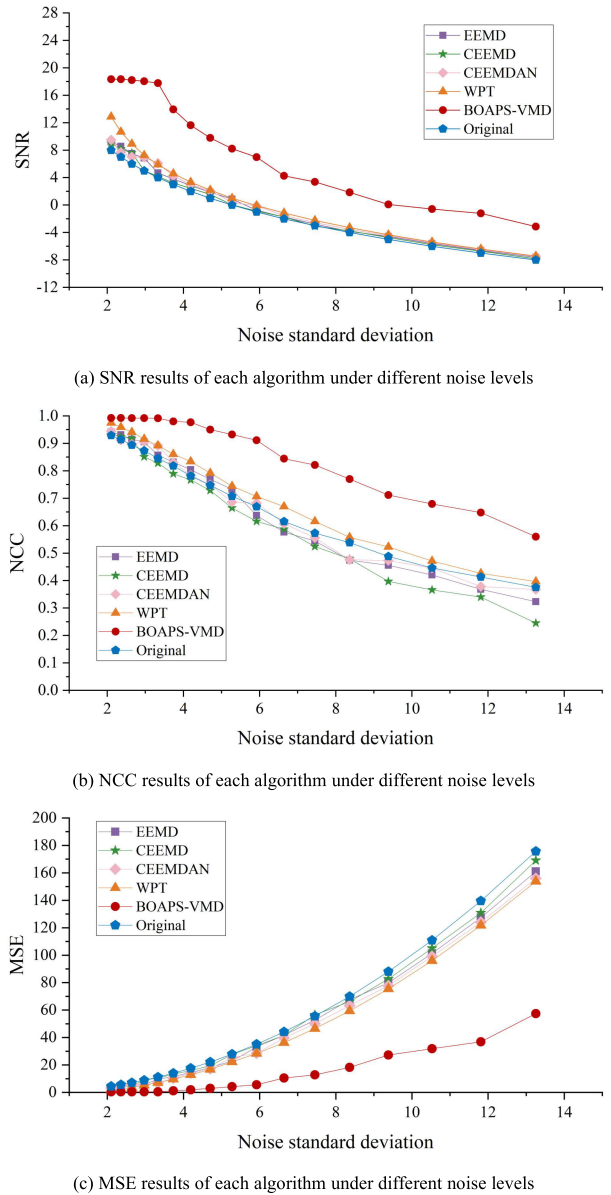

(a) SNR results of each algorithm under different noise levels

(b) NCC results of each algorithm under different noise levels

(c) MSE results of each algorithm under different noise levels

FIGURE 16. Results of SNR, NCC and MSE for each algorithm at different noise levels.

BOAPS-VMD produces higher NCC values than the other algorithms at different noise levels, which is better in preserving the signal signatures. Fig. 16(c) shows the MSE results for each algorithm at different noise standard deviations. Smaller MSE values indicate that the decomposed signal is closer to the original signal and more accurate in retaining signal details. It can be seen that when the maximum value of the noise standard deviation is 13.2533, the maximum MSE value of the original signal is 160.9914, whereas the MSE value of the BOAPS-VMD is 57.3622, which shows that the BOAPS-VMD can effectively reduce the error of the reconstructed signal. Moreover, compared with other algorithms, the MSE between the reconstructed signal and the original signal obtained under the BOAPS-VMD is smaller at the same noise level.

In summary, the following primary conclusions can be drawn from the above analysis:

1. Following the occurrence of ITSC in PMSM, the main fault signature frequency that appears in one of the nonlinear signals (torque fluctuation signal) during motor operation is 100 Hz (2x the rotation frequency).

2. BOAPS-VMD shows better signal adaptive decomposition capability, which improves the modal mixing phenomenon. EEMD, CEEMD, CEEMDAN, and WPT algorithms all show modal mixing in the results of the decomposition, and the influence of noise is significant, which can further affect the identification of fault signature. The C-VCR performs well in identifying the fault signature frequency, which improves the accuracy of fault detection.

3. The evaluation metrics of SNR, NCC, and MSE show that the BOAPS-VMD exhibits better noise robustness compared to the EEMD, CEEMD, CEEMDAN, and WPT algorithms.

V. ENGINEERING CASE ANALYSIS

A. EXPERIMENTAL PLATFORM BUILDING

In this section, an experimental platform for ITSC in PMSM is established. Based on this, this section will further validate the effectiveness and engineering applicability of the proposed BOAPS-VMD. In addition, the effectiveness and accuracy of BOAPS-VMD applied to the detection of ITSC in PMSM will be further validated. The basic parameters of PMSM used in the experiment are given in Table 4. The platform for ITSC in PMSM consists of a computer, three-phase power supply, PMSM, data collector and vibration sensor, which is shown in Fig. 17.

In the experiment, the vibration sensor is attached to the surface of the motor housing and collects the motor vibration data input to the computer. The vibration sensor is a piezoelectric acceleration sensor, type INV9822, with the following main parameters: range 50g, voltage sensitivity 100 mV/g, maximum lateral sensitivity less than 5%, frequency response range 0.5-8kHz. The data collector used in this study is a measurement amplifier, which type is QuantumX MX1601B. This data collector also supplies power to the sensor. In the experiment, the motor is already in stable operation when the vibration signal is collected. After that, the ITSC is set to the stator winding. Finally, the collected data is analyzed using MATLAB.

B. ANALYSIS OF MEASURED VIBRATION SIGNAL

The accuracy of the BOAPS-VMD is further analyzed using the nonlinear signal (vibration signal) collected in the experiment. Fig. 18 shows the vibration signal collected in the experiment. The sampling frequency of the signal is 1200 Hz. Fig. 19 shows the vibration signals from 0s to 5s before the motor fault and 15s to 20s after the motor fault. Fig. 20 shows the spectrograms corresponding to the two signals.

Analysis of Fig. 20 shows that the amplitude of even rotational frequencies such as 100Hz, 200Hz, and 300Hz increases in the vibration signal after the motor fault. The
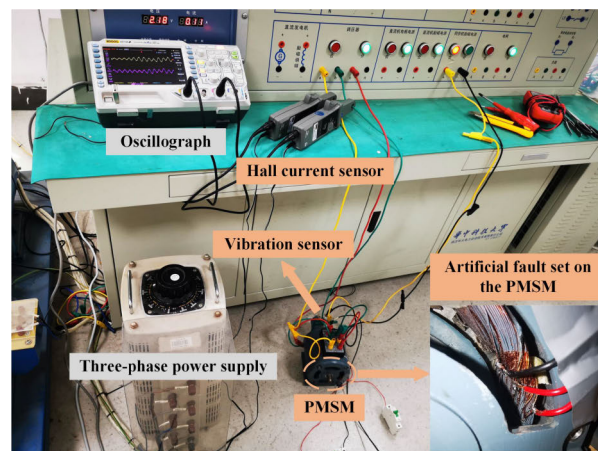
(a) Motor test platform
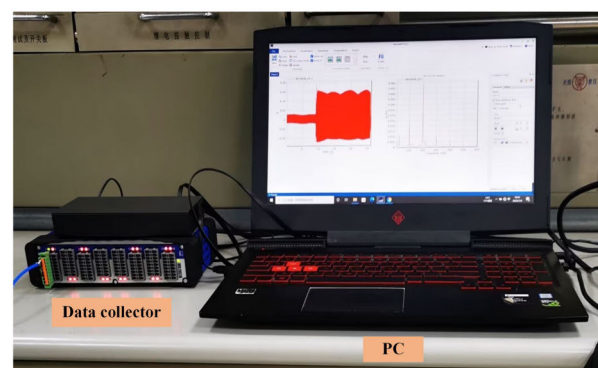
(b) Data collection platform

FIGURE 17. Experimental platform for ITSC in PMSM.

TABLE 4. Basic parameters of PMSM.

Parameter	Numerical value
Rated power (W)	90
Frequency (Hz)	50
Rated voltage (V)	220
Rated speed (rpm)	1500
Rated current (A)	0.35

100Hz and 200Hz frequencies increase in amplitude most significantly and are the main fault signature frequencies. After this, the BOAPS-VMD is used to analyze the signal from 15s to 20s.

Firstly, the EMD algorithm is applied to process the vibration signal and 8 IMFs are obtained, thus assigning an optimization range [4], [16] to the decomposition mode number k. Taking into account the sampling frequency, the optimization range for α is specified as [600, 6000]. Similarly, three independent repeat tests are carried out and the parameters set in each optimization are shown in Table 5. After several iterations of the test, it is found that the minimum value of the evaluation function converges to 1.20. It is worth noting that the convergence curves obtained from the three tests are the same. The results of the parameter
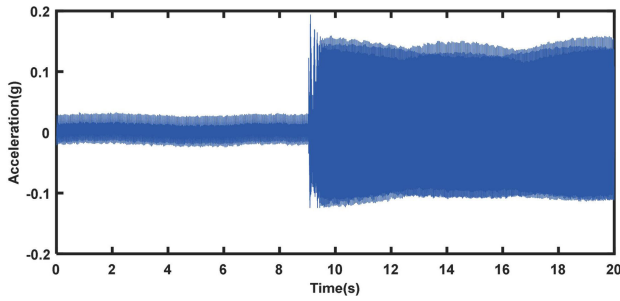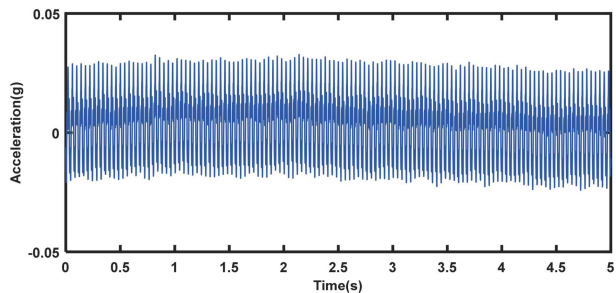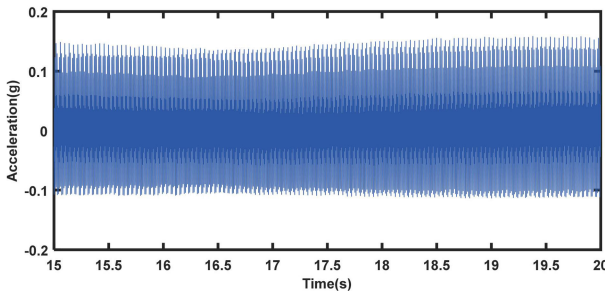
FIGURE 18. Measured vibration signal.
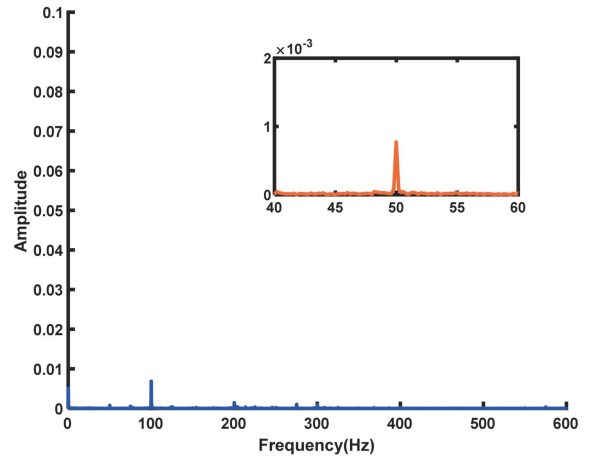

(a) Vibration signal before the fault

(b) Vibration signal after the fault

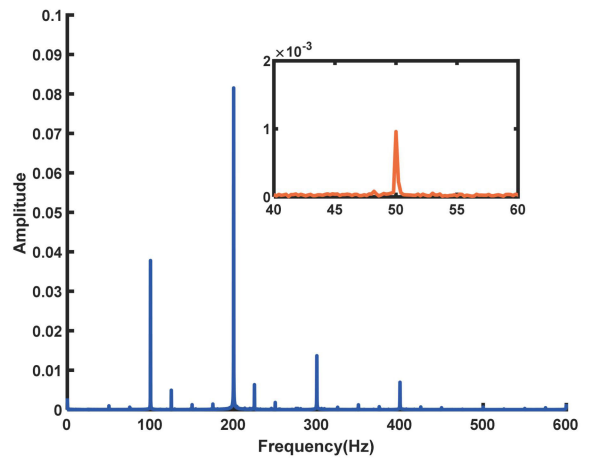**FIGURE 19.** Vibration signals within 0s-5s and 15s-20s.

(a) The spectrogram of the measured vibration signal before the fault

(b) The spectrogram of the measured vibration signal after the fault

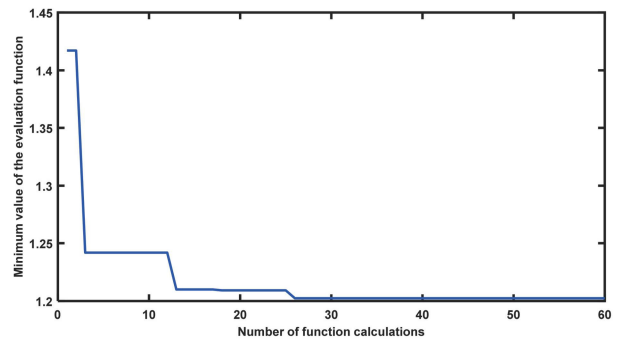**FIGURE 20.** Spectrograms of measured vibration signals.

FIGURE 21. Bayesian optimization convergence curve for measured vibration signal.

combination $[k, \alpha]$ obtained from the three tests are the same. One of the convergence curves is given in the Fig. 21. The processes of Bayesian optimization are shown in Fig. 22.

Finally, the optimal parameter combination obtained by Bayesian optimization is [10, 1592]. The VMD algorithm is used to decompose the vibration signal from 15s to 20s in combination with this parameter combination. The 10 IMFs obtained from the decomposition and the corresponding spectrograms for each IMF are given in Fig. 23. As can be seen in Fig. 23, there is almost no modal mixing occurs in the results, and no over-decomposition phenomenon occurs. In addition, Fig. 23 shows that BOAPS-VMD can better separate the main fault signature frequencies of vibration signal. These results and simulation results all indicate that the BOAPS-VMD can better decompose the signal adaptively, which has certain engineering guidance significance.

Following this, the BOAPS-VMD is combined with HT to detect the ITSC in PMSM. Fig. 24 gives the calculation results of VCR and C-VCR for each IMF in Fig. 23. Similarly, the threshold for C-VCR is set to 90%. According to the results in Fig. 24, IMF6 and IMF8 are fault signature components. These results and simulation results all illustrate that C-VCR shows better fault signature identifying capability. After that, the IMF6 and IMF8 are further analyzed
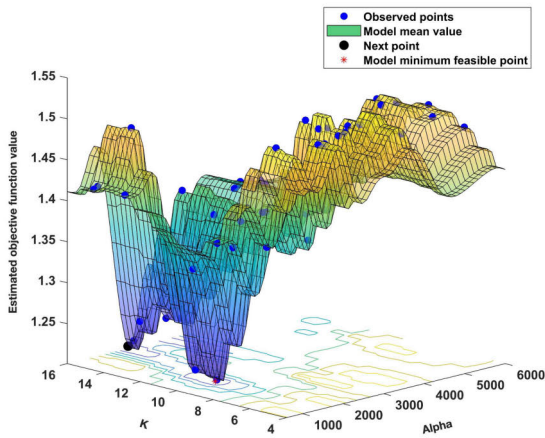
(a) Bayesian optimization process for the 1st test
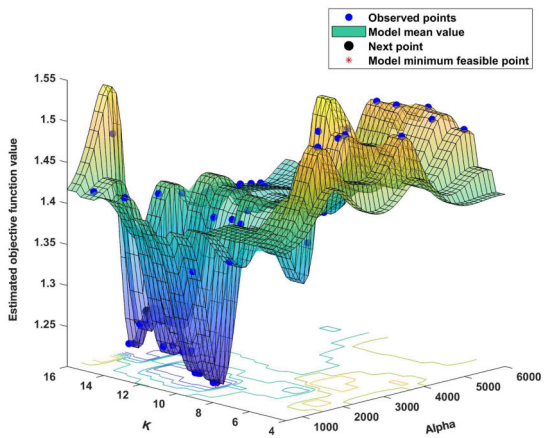
(b) Bayesian optimization process for the 2nd test
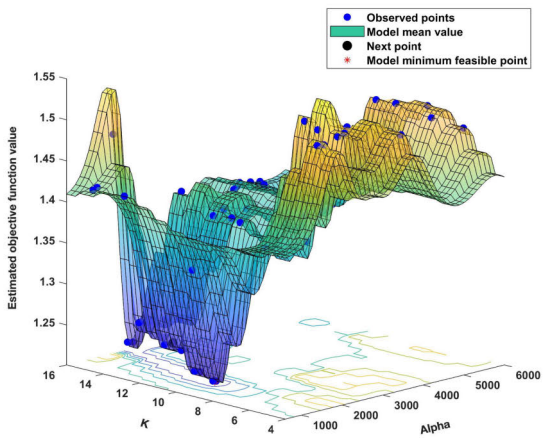
(c) Bayesian optimization process for the 3rd test

FIGURE 22. The processes of Bayesian optimization for measured vibration signal.

with HT. The final results are obtained as shown in Fig. 25. As can be seen from Fig. 25, there is almost no modal
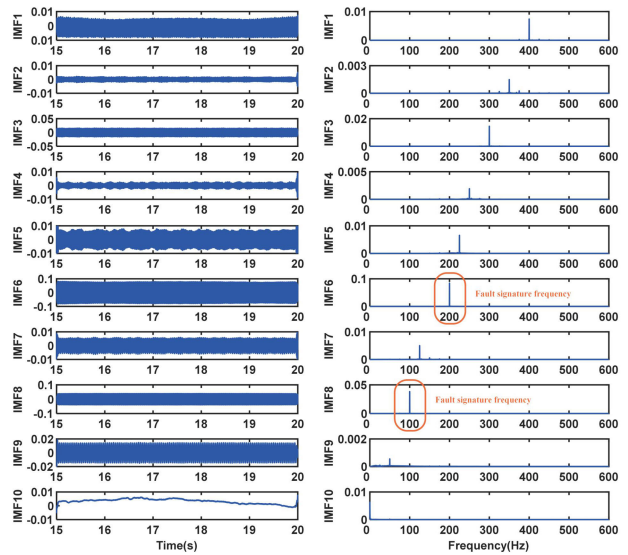

FIGURE 23. Results of BOAPS-VMD decomposition for measured vibration signal.

TABLE 5. Bayesian optimization parameters setting.

Test	MaxObjectiveEvaluations (Iterations)	NumSeedPoints (Points)
1	60	20
2	60	30
3	60	40

mixing phenomenon in the 3D time-frequency diagrams, which can better reflect the fault signatures. However, there is a slight endpoint effect phenomenon appears in the 3D time-frequency diagrams.

The results validate the effectiveness of the proposed BOAPS-VMD applied to detecting the ITSC in PMSM. Similarly, a comparison is given. Two different parameter combinations are set up in the comparison, the first one is $k = 6, \alpha = 1592$; the second one is $k = 10, \alpha = 600$. Afterwards, the VMD algorithm is used to decompose the vibration signal from 15s to 20s in combination with these two sets of parameter combination respectively. Finally, the 3D time-frequency diagrams obtained are given in Fig. 26. Through observation of Fig. 26, there is a slight modal mixing phenomenon appears in the 3D time-frequency diagrams. It is worth noting that, a certain amount of frequency distortion appears in the 3D time-frequency diagrams and a more significant endpoint effect appears in the 3D time-frequency diagrams. These results and simulation results show that BOAPS-VMD has better adaptive signal decomposition ability. Meanwhile, these results also illustrate the necessity of optimizing the VMD algorithm.

After this, EEMD, CEEMD, CEEMDAN, and WPT are combined with HT respectively to analyze the measured vibration signal from 15s to 20s. Finally, the results shown in Fig. 27 are obtained. Analyzing Fig. 27 shows that all of
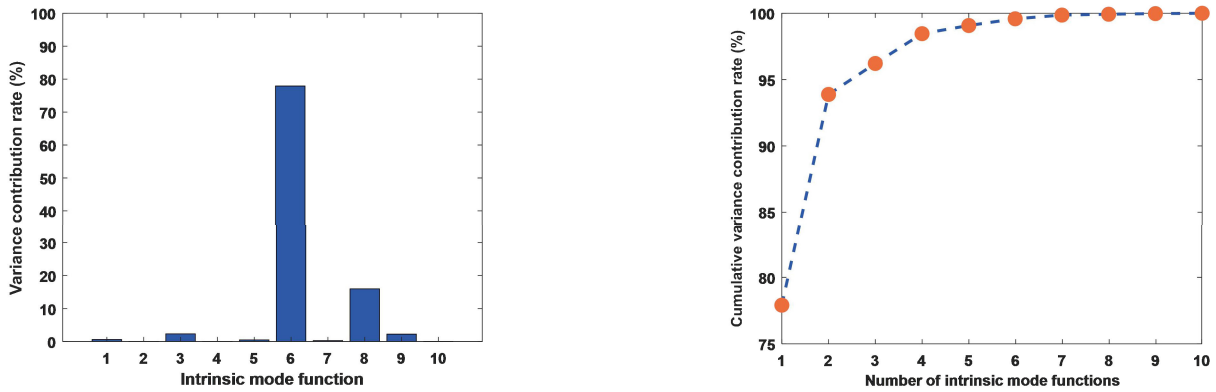
FIGURE 24. Calculation results of VCR and C-VCR for each IMF (Left: VCR; Right: C-VCR).
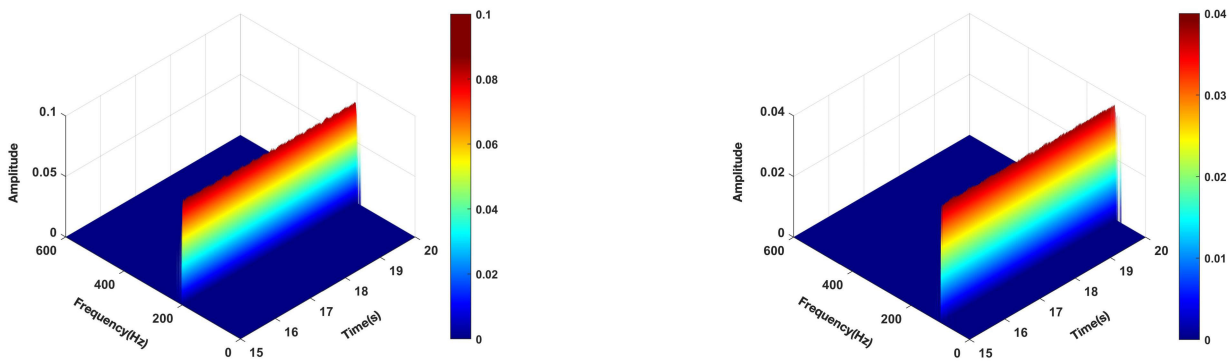

FIGURE 25. 3D time-frequency diagrams obtained from the method proposed in this study.

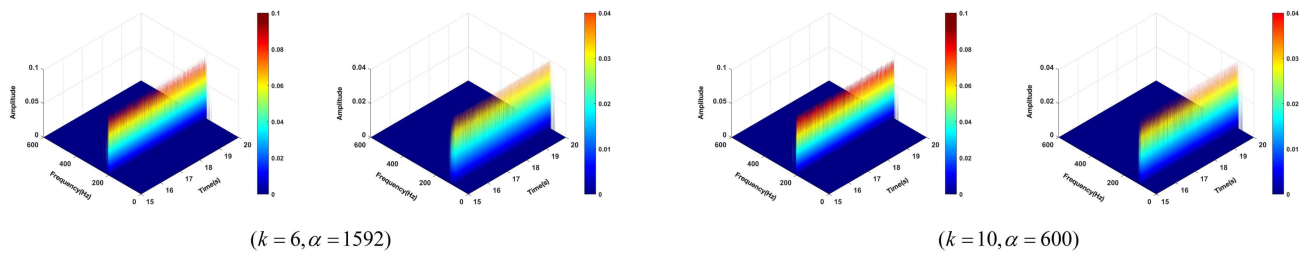$(k = 6, \alpha = 1592)$ $(k = 10, \alpha = 600)$

FIGURE 26. 3D time-frequency diagrams obtained from the VMD algorithm combined with HT under different parameter combinations.

these algorithms in combination with HT are able to detect the ITSC in PMSM. However, the 3D time-frequency diagrams show that the 100Hz and 200Hz fault signature frequencies are almost swamped by other frequencies, which exhibits a significant modal mixing phenomenon. It is worth noting that the motor vibration signal analyzed in this study is measured in the laboratory and the motor operating environment is relatively stable. In practical engineering, the PMSM is usually a component of a particular system.

The vibrations of other components in the system are often included in the vibration signal of PMSM.

Comparing Fig. 25, Fig. 26, and Fig. 27, it can be seen that BOAPS-VMD combined with HT can more accurately detect the ITSC in PMSM, and the endpoint effect phenomenon is improved to some extent. This method shows better noise robustness, which has better engineering guidance significance. It is worth noting that there is always a certain endpoint effect phenomenon in the results of HT. Although the BOAPS-VMD combined with HT proposed in this study can improve the endpoint effect phenomenon to some extent, it cannot eliminate it completely.
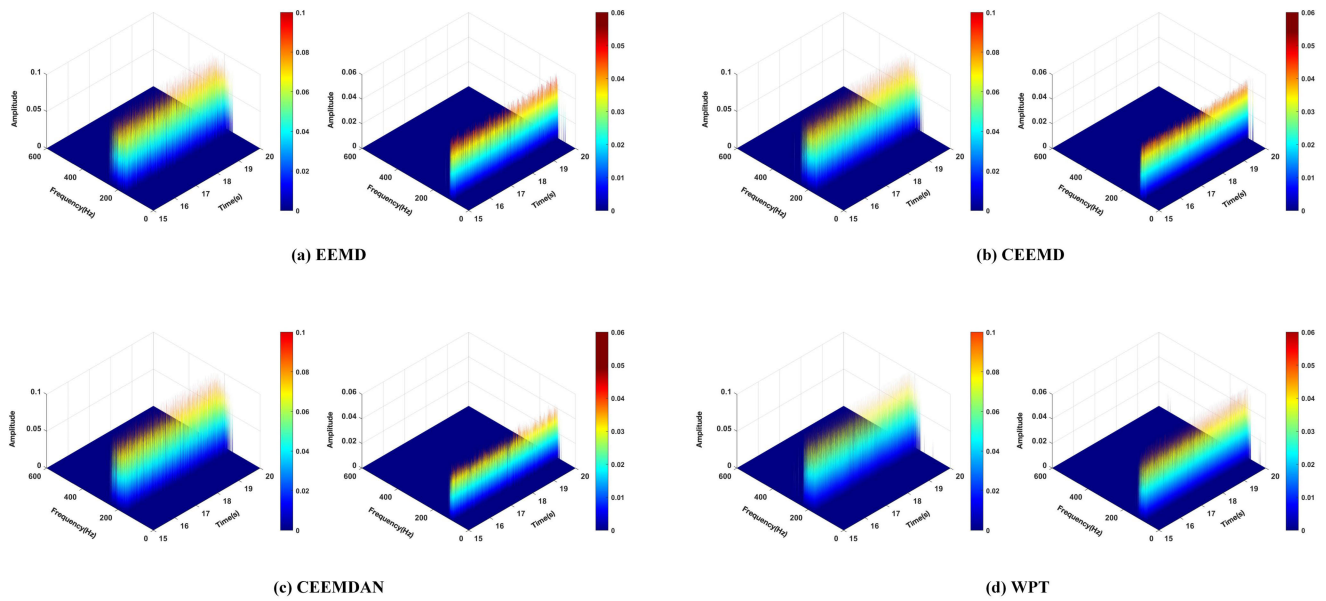
FIGURE 27. 3D time-frequency diagrams obtained by combining the EEMD, CEEMD, CEEMDAN and WPT with HT respectively.
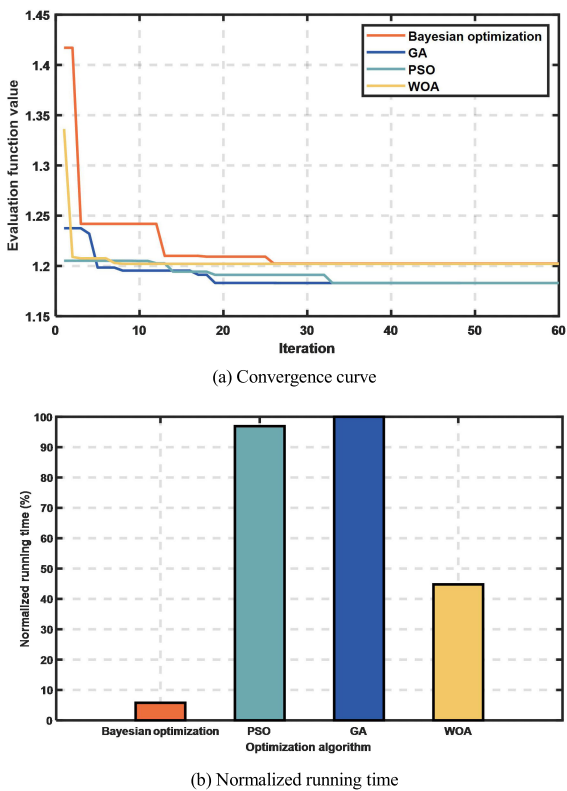

FIGURE 28. Convergence curve and normalized running time for different optimization algorithm.

C. PERFORMANCE ANALYSIS OF OPTIMIZATION ALGORITHMS

In this section, to further analyze the effectiveness and engineering applicability of Bayesian optimization for BOAPS-VMD, the performance of several common optimization algorithms such as PSO [31], GA [32] and WOA [33] are compared. Taking the measured vibration signal from 15s to 20s as an example, Bayesian optimization, PSO, GA, and WOA are used to find the optimal parameter combination for the VMD algorithm respectively. It is worth noting that each optimization algorithm uses the evaluation function proposed in this study, with the same parameter settings for each optimization algorithm. The parameters for Bayesian optimization are set as follows: the iteration number is 60, the point number is 30. The parameters for other optimization algorithms are set as follows: the iteration number is 60, the population number is 30. In addition, the optimization range of k is set as [4] and [16]; the optimization range of α is set as [600, 6000]. The convergence curve and normalized running time for each optimization algorithm are given in Fig. 28.

From Fig. 28(a), it can be seen that Bayesian optimization and WOA exhibit similar convergence values. PSO and GA exhibit similar convergence values. The convergence accuracy of PSO and GA is slightly higher compared to Bayesian optimization and WOA. It is worth noting that Fig. 28(b) shows that Bayesian optimization has the lowest running time. The running time of PSO and GA is almost twice as long as that of WOA. The above analysis shows that the Bayesian optimization used in this study exhibits high search speed with good global search capability in practical application.

After that, the performance of different optimization algorithms applied to the detection of ITSC is analyzed. The optimal parameter combinations for the VMD algorithm searched by Bayesian optimization, PSO, GA and WOA in this study are shown in Table 6.
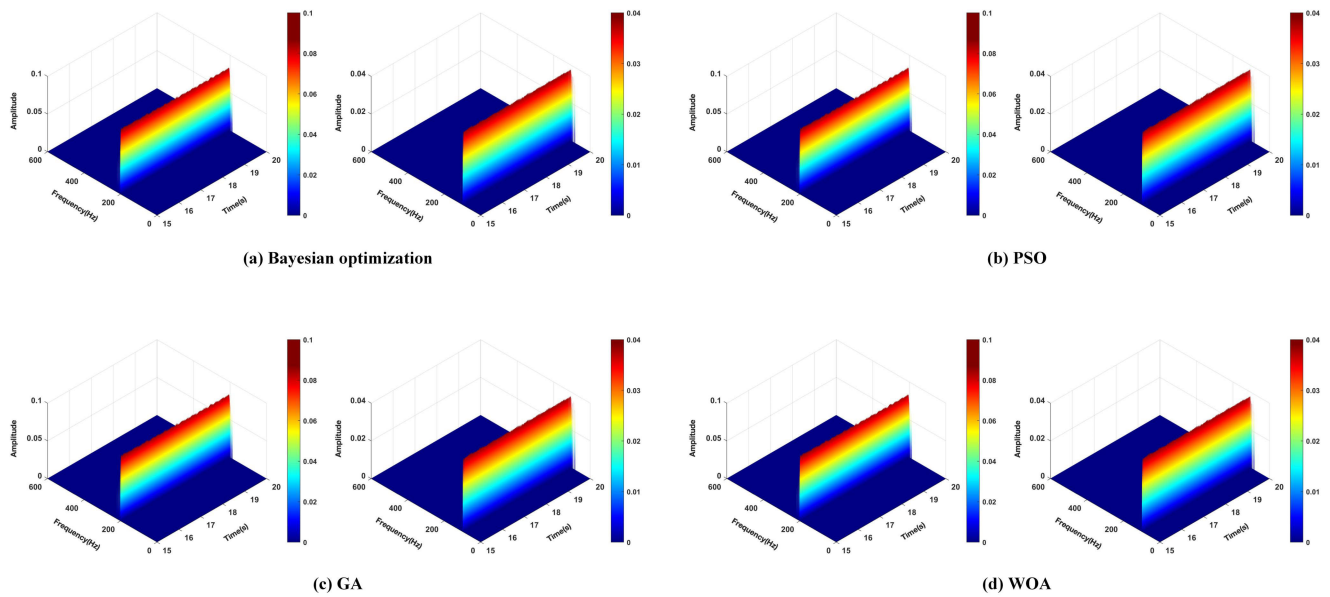
FIGURE 29. 3D time-frequency diagrams obtained from the VMD algorithm combined with HT under different optimal parameter combinations.

TABLE 6. Optimization results for different algorithms.

Algorithm	K	Alpha
Bayesian optimization	10	1592
PSO	11	955
GA	11	957
WOA	10	1637

The different optimal parameter combinations are combined with VMD to decompose the measured vibration signal from 15s to 20s respectively. Finally, the results obtained are shown in Fig. 29. As can be seen from Fig. 29, the different optimization algorithms all show good performance when applied to the detection of ITSC in PMSM. It is worth noting that compared to other optimization algorithms, Bayesian optimization demonstrates higher optimization efficiency. Overall, the method proposed in this study requires lower computational resources and shows good performance in practical engineering application.

VI. CONCLUSION
In this study, the BOAPS-VMD signal processing method is proposed and applied to detect the ITSC in PMSM. Meanwhile, the effectiveness and accuracy are verified through simulation and experiment. There are some conclusions to be drawn:

1. The simulation results indicate that BOAPS-VMD is better able to adaptively decompose the signal compared to EEMD, CEEMD, CEEMDAN and WPT algorithms, which improves the modal mixing phenomenon.

2. Both simulation and experiment results indicate that BOAPS-VMD shows better noise robustness compared to

EEMD, CEEMD, CEEMDAN and WPT, which has better engineering applicability. Meanwhile, the C-VCR performs well in identifying the fault signature components.

3. The experiment results indicate that Bayesian optimization exhibits high search speed with good global search capability in practical application compared to PSO, GA and WOA.

4. The experiment results indicate that BOAPS-VMD combined with HT performs well in detecting the ITSC in PMSM. In addition, the use of 3D time-frequency diagrams for the presentation of results further improves the representation of fault signatures.

It is worth noting that the vibration during operation of a PMSM can be caused not only by an ITSC but also by many other factors. In future work, more measured data would be taken to verify the generalization ability of the method proposed in this study.

REFERENCES
[1] Y. Gao, T. Yang, S. Bozhko, P. Wheeler, T. Dragicevic, and C. Gerada, "Neural network aided PMSM multi-objective design and optimization for more-electric aircraft applications," *Chin. J. Aeronaut.*, vol. 35, no. 10, pp. 233–246, Oct. 2022.

[2] M. Wang and Z. Chen, "Research on permanent magnet structure of permanent magnet synchronous motor for electric vehicle," in *Proc. 2nd Int. Conf. Electr. Eng. Control Sci. (IC2ECS)*, Nanjing, China, Dec. 2022, pp. 990–993.

[3] Y. Lin, M. Xiao, H. Liu, Z. Li, S. Zhou, X. Xu, and D. Wang, "Gear fault diagnosis based on CS-improved variational mode decomposition and probabilistic neural network," *Measurement*, vol. 192, Mar. 2022, Art. no. 110913.

[4] Z. Zheng, Q. Li, X. Li, P. Zheng, K. Wang, and P. Cui, "Analysis and fault-tolerant control of inter-turn short-circuit fault for five-phase permanent-magnet synchronous machine," *Energy Rep.*, vol. 8, pp. 7360–7373, Nov. 2022.

[5] A. Mejia-Barron, G. Tapia-Tinoco, J. R. Razo-Hernandez, M. Valtierra-Rodriguez, and D. Granados-Lieberman, "A neural network-based model for MCSA of inter-turn short-circuit faults in induction motors and its power hardware in the loop simulation," *Comput. Electr. Eng.*, vol. 93, Jul. 2021, Art. no. 107234.

[6] C. H. Park, H. Kim, C. Suh, M. Chae, H. Yoon, and B. D. Youn, "A health image for deep learning-based fault diagnosis of a permanent magnet synchronous motor under variable operating conditions: Instantaneous current residual map," *Rel. Eng. Syst. Saf.*, vol. 226, Oct. 2022, Art. no. 108715.

[7] H. Cherif, A. Benakcha, I. Laib, S. E. Chehaidia, A. Menacer, B. Soudan, and A. G. Olabi, "Early detection and localization of stator inter-turn faults based on discrete wavelet energy ratio and neural networks in induction motor," *Energy*, vol. 212, Dec. 2020, Art. no. 118684.

[8] N. Yassa and M. Rachek, "Modeling and detecting the stator winding inter turn fault of permanent magnet synchronous motors using stator current signature analysis," *Math. Comput. Simul.*, vol. 167, pp. 325–339, Jan. 2020.

[9] C. Zeng, S. Huang, J. Lei, Z. Wan, and Y. Yang, "Online rotor fault diagnosis of permanent magnet synchronous motors based on stator tooth flux," *IEEE Trans. Ind. Appl.*, vol. 57, no. 3, pp. 2366–2377, May 2021.

[10] M. Zafarani, E. Bostanci, Y. Qi, T. Goktas, and B. Akin, "Interturn short-circuit faults in permanent magnet synchronous machines: An extended review and comprehensive analysis," *IEEE J. Emerg. Sel. Topics Power Electron.*, vol. 6, no. 4, pp. 2173–2191, Dec. 2018.

[11] Y. Zhang, J. Wu, X. Hong, and Y. He, "Short-circuit fault detection in laminated long stators of high-speed Maglev track based on fractal dimension," *Measurement*, vol. 176, May 2021, Art. no. 109177.

[12] A. Almounajjed, A. K. Sahoo, and M. K. Kumar, "Diagnosis of stator fault severity in induction motor based on discrete wavelet analysis," *Measurement*, vol. 182, Sep. 2021, Art. no. 109780.

[13] D. K. Ray, T. Roy, and S. Chattopadhyay, "Skewness scanning for diagnosis of a small inter-turn fault in quadcopter's motor based on motor current signature analysis," *IEEE Sensors J.*, vol. 21, no. 5, pp. 6952–6961, Mar. 2021.

[14] Y. Qi, E. Bostanci, M. Zafarani, and B. Akin, "Severity estimation of interturn short circuit fault for PMSM," *IEEE Trans. Ind. Electron.*, vol. 66, no. 9, pp. 7260–7269, Sep. 2019.

[15] X. Wang, Z. Liu, L. Zhang, and W. P. Heath, "Wavelet package energy transmissibility function and its application to wind turbine blade fault detection," *IEEE Trans. Ind. Electron.*, vol. 69, no. 12, pp. 13597–13606, Dec. 2022.

[16] Y. Xia, X. Li, and Y. Luo, "Inter-turn short circuit fault detection of PMSM based on wavelet packet energy spectrum and CEEMDAN-HT," *J. Electr. Eng. Technol.*, Aug. 2023.

[17] R. Z. Haddad and E. G. Strangas, "On the accuracy of fault detection and separation in permanent magnet synchronous machines using MCSA/MVSA and LDA," *IEEE Trans. Energy Convers.*, vol. 31, no. 3, pp. 924–934, Sep. 2016.

[18] H. Talhaoui, A. Menacer, A. Kessal, and R. Kechida, "Fast Fourier and discrete wavelet transforms applied to sensorless vector control induction motor for rotor bar faults diagnosis," *ISA Trans.*, vol. 53, no. 5, pp. 1639–1649, Sep. 2014.

[19] Y. Li, B. Tang, S. Jiao, and Y. Zhou, "Optimized multivariate multiscale slope entropy for nonlinear dynamic analysis of mechanical signals," *Chaos, Solitons Fractals*, vol. 179, Feb. 2024, Art. no. 114436.

[20] Y. Li, S. Jiao, S. Deng, B. Geng, and Y. Li, "Refined composite variable-step multiscale multimapping dispersion entropy: A nonlinear dynamical index," *Nonlinear Dyn.*, vol. 112, no. 3, pp. 2119–2137, Feb. 2024.

[21] Y. Li, B. Tang, S. Jiao, and Q. Su, "Snake optimization-based variable-step multiscale single threshold slope entropy for complexity analysis of signals," *IEEE Trans. Instrum. Meas.*, vol. 72, pp. 1–13, 2023.

[22] X. Zhu, S. Li, Y. Guo, X. Chen, C. He, and J. Deng, "Novel wavefront detection and fault location method based on Hilbert-huang transform for long HVDC transmission lines," *Electric Power Syst. Res.*, vol. 211, Oct. 2022, Art. no. 108213.

[23] Q. Wang, P. Geng, J. Chen, and C. He, "Dynamic discrimination method of seismic damage in tunnel portal based on improved wavelet packet transform coupled with Hilbert-huang transform," *Mech. Syst. Signal Process.*, vol. 188, Apr. 2023, Art. no. 110023.

[24] Z. Liu, D. Peng, M. J. Zuo, J. Xia, and Y. Qin, "Improved Hilbert–Huang transform with soft sifting stopping criterion and its application to fault diagnosis of wheelset bearings," *ISA Trans.*, vol. 125, pp. 426–444, Jun. 2022.

[25] N. E. Huang, Z. Shen, S. R. Long, M. C. Wu, H. H. Shih, Q. Zheng, N.-C. Yen, C. C. Tung, and H. H. Liu, "The empirical mode decomposition and the Hilbert spectrum for nonlinear and non-stationary time series analysis," *Proc. Roy. Soc. London. Ser. A, Math., Phys. Eng. Sci.*, vol. 454, no. 1971, pp. 903–995, Mar. 1998.

[26] J. Zheng, M. Su, W. Ying, J. Tong, and Z. Pan, "Improved uniform phase empirical mode decomposition and its application in machinery fault diagnosis," *Measurement*, vol. 179, Jul. 2021, Art. no. 109425.

[27] J. Zheng, J. Cheng, and Y. Yang, "Partly ensemble empirical mode decomposition: An improved noise-assisted method for eliminating mode mixing," *Signal Process.*, vol. 96, pp. 362–374, Mar. 2014.

[28] L. Wang and Y. Shao, "Fault feature extraction of rotating machinery using a reweighted complete ensemble empirical mode decomposition with adaptive noise and demodulation analysis," *Mech. Syst. Signal Process.*, vol. 138, Apr. 2020, Art. no. 106545.

[29] H. Zhou, P. Yan, Y. Yuan, D. Wu, and Q. Huang, "Denoising the hob vibration signal using improved complete ensemble empirical mode decomposition with adaptive noise and noise quantization strategies," *ISA Trans.*, vol. 131, pp. 715–735, Dec. 2022.

[30] K. Dragomiretskiy and D. Zosso, "Variational mode decomposition," *IEEE Trans. Signal Process.*, vol. 62, no. 3, pp. 531–544, Feb. 2014.

[31] X.-B. Wang, Z.-X. Yang, and X.-A. Yan, "Novel particle swarm optimization-based variational mode decomposition method for the fault diagnosis of complex rotating machinery," *IEEE/ASME Trans. Mechatronics*, vol. 23, no. 1, pp. 68–79, Feb. 2018.

[32] J. Li, W. Chen, K. Han, and Q. Wang, "Fault diagnosis of rolling bearing based on GA-VMD and improved WOA-LSSVM," *IEEE Access*, vol. 8, pp. 166753–166767, 2020.

[33] Y. Wang, S. Zhang, R. Cao, D. Xu, and Y. Fan, "A rolling bearing fault diagnosis method based on the WOA-VMD and the GAT," *Entropy*, vol. 25, no. 6, p. 889, Jun. 2023.

[34] X. Ji, Z. Tian, H. Song, and F. Liu, "Structural performance degradation identification of offshore wind turbines based on variational mode decomposition with a grey wolf optimizer algorithm," *Ocean Eng.*, vol. 256, Jul. 2022, Art. no. 111449.

[35] J. Wang, C. Zhan, S. Li, Q. Zhao, J. Liu, and Z. Xie, "Adaptive variational mode decomposition based on archimedes optimization algorithm and its application to bearing fault diagnosis," *Measurement*, vol. 191, Mar. 2022, Art. no. 110798.

[36] N. Basha, C. Kravaris, H. Nounou, and M. Nounou, "Bayesian-optimized Gaussian process-based fault classification in industrial processes," *Comput. Chem. Eng.*, vol. 170, Feb. 2023, Art. no. 108126.

[37] S. Tang, Y. Zhu, and S. Yuan, "Intelligent fault diagnosis of hydraulic piston pump based on deep learning and Bayesian optimization," *ISA Trans.*, vol. 129, pp. 555–563, Oct. 2022.

[38] Y. Xia and W. Tang, "Study on the estimation of harmonic impedance based on Bayesian optimized Gaussian process regression," *Int. J. Electr. Power Energy Syst.*, vol. 142, Nov. 2022, Art. no. 108294.

[39] C. Xu, J. Yang, T. Zhang, K. Li, and K. Zhang, "Adaptive parameter selection variational mode decomposition based on a novel hybrid entropy and its applications in locomotive bearing diagnosis," *Measurement*, vol. 217, Aug. 2023, Art. no. 113110.

[40] J. Sun, Q. Xiao, J. Wen, and F. Wang, "Natural gas pipeline small leakage feature extraction and recognition based on LMD envelope spectrum entropy and SVM," *Measurement*, vol. 55, pp. 434–443, Sep. 2014.

[41] H. Yu, H. Li, and Y. Li, "Vibration signal fusion using improved empirical wavelet transform and variance contribution rate for weak fault detection of hydraulic pumps," *ISA Trans.*, vol. 107, pp. 385–401, Dec. 2020.

[42] M. Aishwarya and R. M. Brisilla, "Design of energy-efficient induction motor using ANSYS software," *Results Eng.*, vol. 16, Dec. 2022, Art. no. 100616.

[43] M. Dems and K. Komeza, "Performance characteristics of a high-speed energy-saving induction motor with an amorphous stator core," *IEEE Trans. Ind. Electron.*, vol. 61, no. 6, pp. 3046–3055, Jun. 2014.

[44] S. Balci and M. Akkaya, "Reduction of the core size and power losses by using soft magnetic material for a single-phase induction motor," *Measurement*, vol. 198, Jul. 2022, Art. no. 111421.

[45] Y.-K. Xia and X.-Y. Li, "Calculation and experiment of stray inductance of PCB double-pulse test circuit based on three-dimensional simulation," *IEEE Access*, vol. 10, pp. 58769–58776, 2022.

[46] K. Wen, L. Han, Z.-T. Zhou, Z.-N. Fan, Y. Liao, J. Wang, Z. Sun, B. Yao, and B.-D. Zhang, "3D electromagnetic-temperature field close-coupling calculation of losses and heat in the damper winding of a large tubular hydro-generator," *J. Electr. Eng. Technol.*, vol. 14, no. 3, pp. 1255–1268, May 2019.

[47] Z.-N. Fan, Z.-Y. Bian, K. Xiao, J.-C. Li, B. Yao, and X.-G. Gan, "The electromagnetic-fluid-temperature field analysis of loss and heat of self-cooling separate-phase enclosed bus of large generator," *IEEE Access*, vol. 9, pp. 11372–11377, 2021.

WAN-TING WANG was born in Sichuan, China, in 2000. She received the B.S. degree in electrical engineering from Xihua University, in 2022, where she is currently pursuing the M.S. degree in electrical engineering with the Department of Electrical Engineering. Her research interests include signal processing and fault detection.

YAN-KUN XIA was born in Hubei, China, in 1984. He received the Ph.D. degree from Southwest Jiaotong University, Chengdu, China, in 2014. He is currently an Associate Professor with Xihua University. He is also a Researcher with the Traction Power State Key Laboratory, Southwest Jiaotong University. His research interests include modeling, Simulink, and measurement of power system and new technology.
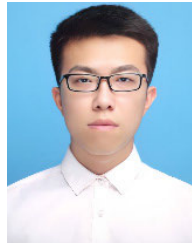
XIN-YANG LI was born in Sichuan, China, in 1998. He received the B.S. degree in electrical engineering from Xihua University, in 2020, where he is currently pursuing the M.S. degree in electrical engineering with the Department of Electrical Engineering. His research interests include power systems and power quality analysis.

● ● ●